

The quenching of the star formation activity in cluster galaxies

A. Boselli^{1*}, Y. Roehlly¹, M. Fossati^{2,3}, V. Buat¹, S. Boissier¹, M. Boquien⁴, D. Burgarella¹, L. Ciesla⁵, G. Gavazzi⁶, P. Serra⁷

¹ Aix Marseille Université, CNRS, LAM (Laboratoire d'Astrophysique de Marseille), UMR 7326, F-13388, Marseille, France e-mail: alessandro.boselli@lam.fr, yannick.roehlly@lam.fr, veronique.buat@lam.fr, samuel.boissier@lam.fr, denis.burgarella@lam.fr

² Universitäts-Sternwarte München, Scheinerstrasse 1, D-81679 München, Germany

³ Max-Planck-Institut für Extraterrestrische Physik, Giessenbachstrasse, 85748, Garching, Germany e-mail: mfossati@mpe.mpg.de

⁴ Unidad de Astronomia, Universidad de Antofagasta e-mail: mederic.boquien@uantof.cl

⁵ Laboratoire AIM-Paris-Saclay, CEA/DSM/Irfu - CNRS - Université Paris Diderot, CEA-Saclay, 91191, Gif-sur-Yvette, France e-mail: laure.ciesla@cea.fr

⁶ Università di Milano-Bicocca, piazza della scienza 3, 20100, Milano, Italy e-mail: giuseppe.gavazzi@mib.infn.it

⁷ CSIRO Astronomy and Space Science, Australia Telescope National Facility, PO Box 76, Epping, NSW 1710, Australia e-mail: paolo.serra@csiro.au

ABSTRACT

We study the star formation quenching mechanism in cluster galaxies by fitting the spectral energy distribution of the *Herschel* Reference Survey, a complete volume-limited *K*-band-selected sample of nearby galaxies including objects in different density regions, from the core of the Virgo cluster to the general field. The spectral energy distributions of the target galaxies are fitted using the CIGALE SED modelling code. The truncated activity of cluster galaxies is parametrised using a specific star formation history with two free parameters, the quenching age QA and the quenching factor QF . These two parameters are crucial for the identification of the quenching mechanism which acts on long timescales if starvation while rapid and efficient if ram pressure. To be sensitive to an abrupt and recent variation of the star formation activity, we combine in a new way twenty UV to far infrared photometric bands with three age-sensitive Balmer line absorption indices extracted from available medium-resolution ($R \sim 1000$) integrated spectroscopy and with $H\alpha$ narrow band imaging data. The use of a truncated star formation history significantly increases the quality of the fit in HI-deficient galaxies of the sample, thus in those objects whose atomic gas content has been removed during the interaction with the hostile cluster environment. The typical quenching age of the perturbed late-type galaxies is $QA \lesssim 300$ Myr whenever the activity of star formation is reduced by $50\% < QF \leq 80\%$ and $QA \lesssim 500$ Myr for $QF > 80\%$, while that of the quiescent early-type objects is $QA \approx 1-3$ Gyr. The fraction of late-type galaxies with a star formation activity reduced by $QF > 80\%$ and with an HI-deficiency parameter $HI - def > 0.4$ drops by a factor of ~ 5 from the inner half virial radius of the Virgo cluster ($R/R_{vir} < 0.5$), where the hot diffuse X-ray emitting gas of the cluster is located, to the outer regions ($R/R_{vir} > 4$). The efficient quenching of the star formation activity observed in Virgo suggests that the dominant stripping process is ram pressure. We discuss the implication of this result in the cosmological context of galaxy evolution.

Key words. galaxies: clusters: general, galaxies: clusters: individual: Virgo, galaxies: evolution, galaxies: interactions, galaxies: ISM, galaxies: star formation

1. Introduction

Environment plays a major role in shaping galaxy evolution. Since the seminal work of Dressler (1980) it became evident that galaxies in rich environments are systematically different than those located in the field. Dense environments are dominated by early-type galaxies, while low density regions by spirals and irregulars (e.g. Dressler 1980; Whitmore et al. 1993; Dressler et al. 1997). It has also been shown that massive local clusters are currently accreting gas-rich, star forming systems (e.g. Tully & Shaya 1984; Colless & Dunn 1996) whose physical properties systematically change once they reach the densest regions. Indeed, it is now widely recognised that late-type galaxies located in rich clusters are generally HI-deficient (Haynes et al. 1984; Gavazzi 1987; Cayatte et al. 1990; Solanes et al. 2001; Gavazzi et al. 2005, 2006a). There is a growing evidence indicat-

ing that they also lack of molecular gas (Fumagalli et al. 2009; Boselli et al. 2014b) and dust (Cortese et al. 2012a) with respect to similar objects in the field. The angular resolution of the HI, CO, and far infrared images now available thanks to interferometric observations in the radio domain and to the superior quality of the instruments on board of *Herschel* revealed that cluster galaxies have truncated gaseous and dust discs (Fumagalli et al. 2009, Boselli et al. 2014b, Cortese et al. 2012a, Davis et al. 2013), suggesting that the mechanism responsible for their stripping acts outside in. The activity of star formation of the late-type galaxies in clusters is also systematically reduced with respect to that of field objects (Kennicutt 1983; Gavazzi et al. 1998, 2002a, 2006b) and it is limited to the inner disc (Koopmann & Kenney 2004; Boselli & Gavazzi 2006; Cortese et al. 2012b; Fossati et al. 2013). The correlation between the molecular gas content and the activity of star formation (e.g. Bigiel et al. 2008), generally called Schmidt law (Schmidt 1959; Kennicutt 1998a), can easily explain the observed truncation of the star forming discs of these perturbed objects.

* Visiting astronomer at CSIRO Astronomy and Space Science, Australia Telescope National Facility, PO Box 76, Epping, NSW 1710, Australia

Different mechanisms have been proposed in the literature to explain the transformation of galaxies in rich environments and the formation of the red sequence (e.g. Boselli & Gavazzi 2006, 2014). They include the gravitational interaction between galaxies (Merritt 1983) or that with the potential well of the cluster as a whole (Byrd & Valtonen 1990), or their combined effect generally called “galaxy harassment” (Moore et al. 1998). Other possible mechanisms are those related to the interaction of the galaxy interstellar medium with the hot ($T \sim 10^7\text{-}10^8$ K) and dense ($\rho_{\text{ICM}} \sim 10^{-3} \text{ cm}^{-3}$) diffuse gas trapped within the potential well of the clusters observable in X-rays (Sarazin et al. 1986). These include the ram pressure (Gunn & Gott 1972) and the viscous stripping (Nulsen 1982) exerted by the intracluster medium on galaxies moving at high velocity ($\sim 1000 \text{ km s}^{-1}$) within the cluster, or the thermal heating of the galaxy ISM once in contact with the hot X-ray emitting gas of the cluster (Cowie & Songaila 1977). Since a large fraction of cluster galaxies is accreted via small groups, the perturbing mechanisms can start to shape galaxy evolution well before the galaxy is within the massive cluster (pre-processing, e.g. Dressler 2004). Finally, it is possible that under some circumstances the ICM only perturbs the hot gas in the galaxy halo unaffected the cold component on the disc. The cold component, however, not replenished by fresh infalling material, is later exhausted by the star formation activity of the galaxy itself (starvation; Larson et al. 1980).

The identification of the perturbing mechanism responsible for the quenching of the star formation activity of galaxies in high density regions is becoming one of the major challenges of modern extragalactic astronomy. The identification of the dominant perturbing mechanism, which is expected to change with the mass of galaxies and with the properties of the overdensity region, is crucial for cosmological simulations and semi analytical models of galaxy evolution. Different mechanisms may have different effects on the morphology and internal dynamics of the stellar component, making discs thicker and increasing the bulge-to-disc ratio (gravitational perturbations), while other are expected to decrease the surface brightness of the perturbed disc (starvation). At present, models and simulations often overestimate the fraction of quiescent galaxies along the red sequence (Kang & van den Bosch 2008; Font et al. 2008; Kimm et al. 2009; Fontanot et al. 2009; Guo et al. 2011; Weinmann et al. 2011; Wang et al. 2012; Hirschmann et al. 2014; see however Henriques et al. 2015), suggesting that the physical prescriptions used to reproduce the environmental quenching is still poorly understood. An accurate identification of the dominant mechanism is also crucial for the physical understanding of the stripping process, for the calibration of tuned hydrodynamic simulations, and for the characterisation of the effects that the mechanism has on perturbed galaxies and on the stripped material.

Critical for constraining the perturbing mechanism is the identification with observations of its acting radius within high-density regions and of the quantification of the timescale necessary to significantly remove the gas and affect the star formation process (efficiency). The analysis of nearby and high redshift clusters still gives discordant results. The detailed study of representative objects in nearby clusters such as Virgo and Coma based on dynamical modelling of their HI and CO gas kinematics (e.g. Vollmer et al. 2004), of the radial variation of their star formation properties derived from integral field unit (IFU) optical spectroscopy (e.g. Crowl & Kenney 2008), or by the comparison of multifrequency data with tuned chemospectrophotometric models of galaxy evolution (e.g. Boselli et al. 2006) indicate a recent and rapid truncation of their star formation activity consistent with a ram pressure stripping scenario.

The analysis of large statistical samples of galaxies extracted from several surveys such as the SDSS, GAMA, or GALEX, or targeted observations of nearby clusters and groups combined with the results of cosmological simulations or semi analytical models of galaxy evolution rather suggest a slow and long quenching process typical of starvation (McGee et al. 2009; Wolf et al. 2009; von der Linden et al. 2010; De Lucia et al. 2012; Wheeler et al. 2014; Taranu et al. 2014; Haines et al. 2015; Paccagnella et al. 2016). Other works suggest a bimodal evolution, with an inefficient quenching at early epochs, when galaxies become satellites of more massive halos, and then a rapid quenching when these still relative small systems are accreted in massive clusters (pre-processing; e.g. Wetzel et al. 2012, 2013; Muzzin et al. 2012; Wijesinghe et al. 2012).

The identification of the perturbing mechanism requires an accurate reconstruction of the star formation history of galaxies in different environments. This is generally done using photometric and spectroscopic data to characterise the stellar emission in the UV to near-infrared spectral domain. The typical colours of galaxies in these bands are sensitive to their underlying stellar populations, and become redder whenever the star formation activity decreases because perturbed by the surrounding environment. The reconstruction of the star formation history of perturbed galaxies using these sets of data, however, is limited by the fact that other physical mechanisms such as dust attenuation and metallicity might affect the colours of galaxies in a similar way. To overcome this problem and limit any possible degeneracy between the effects of dust attenuation and aging of the stellar populations astronomers developed UV to far-infrared spectral energy distribution (SED) fitting codes. These codes, by measuring the total energy emitted by dust in the far-infrared, are able to quantify in a self consistent way the dust attenuation on the stellar emission, and are thus now widely used to study the star formation history of different samples of galaxies (e.g. GRASIL: Silva et al. 1998; MAGPHYS: da Cunha et al. 2008).

In the last years a huge number of multifrequency data, from the UV to the radio centimetre, have been gathered for a complete volume-limited sample of nearby galaxies, the *Herschel* Reference Survey (HRS). This sample includes galaxies in different density regions, from the core of the Virgo cluster to the general field, and is thus perfectly suited for environmental studies (Boselli et al. 2010a). These data are perfectly suited to be fitted with CIGALE, a modelling code designed to reconstruct the star formation history of galaxies through an analysis of their UV to far infrared SED (Noll et al. 2009). In this work we improve this SED fitting code to combine in an original manner twenty photometric bands imaging data with three age sensitive spectroscopic indices (Balmer absorption lines) derived from integrated spectroscopy (Boselli et al. 2013) and narrow band H α imaging data (Boselli et al. 2015) with the aim of characterising the quenching star formation episode. We already explored the use of the SED fitting analysis to reproduce the variations on the star formation history of cluster galaxies using only broad band imaging photometry in Ciesla et al. (2016). The present work is thus a further development of this technique. To date the combination of photometric and spectroscopic data in the SED fitting analysis has been limited to the stellar emission (Pacifci et al. 2012, 2015; Newman et al. 2014; Thomas et al. 2016; Chevillard & Charlot 2016; Lopez Fernandez et al. 2016). Our work is the first where this technique is extended to a much wider spectral domain, from the UV to the far-infrared, where the far-infrared emission is used through an energy balance to break any possible degeneracy due to dust attenuation in the observed stellar emission. The paper is structured as follow: we describe the sample

in sect. 2, the multifrequency data in sect. 3, and the SED fitting technique and procedure in sect. 4. Section 4 also includes several tests done on mock samples to check the reliability of the output parameters. In sect. 5 we apply the SED fitting code to a dozen of representative galaxies for which independent results are available in the literature, and in sect. 6 to the whole HRS sample. The analysis is done in sect. 7 and the discussion in sect. 8. In Appendix A we discuss the effects of the adoption of different star formation histories on the derived quenching parameters. For a fair comparison with models and simulations we recall that the typical distance of the main body of the Virgo cluster is 17 Mpc (Gavazzi et al. 1999; Mei et al. 2007) and its total dynamical mass $M_{200} (1.4-4.2) \times 10^{14} M_{\odot}$ (McLaughlin 1999; Urban et al. 2011; Nulsen & Bohringer 1995; Schindler et al. 1999).

2. The sample

The sample analysed in this work has been extracted from the *Herschel* Reference Survey (HRS; Boselli et al. 2010a). The HRS is a volume-limited ($15 \leq D \leq 25$ Mpc), *K*-band-selected (2MASS $K \leq 12$ mag for late-type galaxies, $K \leq 8.7$ mag for early-type ellipticals and lenticulars) complete sample of 322 nearby galaxies. As selected, the sample spans a wide range in morphological type (E-S0-Spirals-BCDs-Im, see Table 1) and stellar mass ($10^8 \leq M_{star} \leq 10^{11} M_{\odot}$), making the HRS a statistically representative stellar mass selected sample of the nearby universe (Boselli et al. 2010a). The spectrophotometric data required for this analysis are available for 168/260 late-type galaxies of the sample, while only for 22/62 early-type galaxies (6/19 E, 15/36 S0, 1/4 S0a)¹. The sample is ideally suited for environmental studies because it includes galaxies in a wide range of densities, from the dense core of the Virgo cluster to small groups, binary systems and relatively isolated objects in the field. Strong observational evidence has been collected so far indicating that the HRS galaxies in the Virgo cluster have been perturbed by their interaction with the hostile environment (Cortese et al. 2010, 2011, 2012a, 2012b, 2016; Boselli et al. 2014b, 2015). Although a few galaxies have a nuclear activity (Gavazzi et al. in prep.), the contribution of the AGN to the integrated spectrum is negligible (Boselli et al. 2013). The HRS is also ideally defined because it includes a large number of well studied Virgo cluster galaxies where the comparison of their kinematic and spectrophotometric properties have been crucial for the identification of the perturbing process and dating the epoch of the first interaction with the hostile environment (Vollmer et al. 1999, 2000, 2004, 2005, 2006, 2008a, 2008b, 2009, 2012; Vollmer 2003; Kenney et al. 2004; Boselli et al. 2005, 2006; Crowl & Kenney 2008; Abramson et al. 2011; Kenney et al. 2014; Abramson & Kenney 2014; Cortes et al. 2015).

3. The data

The HRS is perfectly suited for an SED analysis because photometric and spectroscopic data covering the whole electromagnetic spectrum are available for all galaxies. All photometric and spectroscopic data are integrated quantities and thus do not deserve any aperture correction, a probable source of systematic effects in perturbed galaxies given the outside-in truncation of the star forming disc. The objects analysed in this work have been

¹ We exclude from the following analysis the radio galaxies M87 (Virgo A) and M84 because their far infrared emission is due to synchrotron (Baes et al. 2010; Boselli et al. 2010b, 2012).

Table 1. The morphological distribution of the HRS.

Type	HRS	analysed galaxies ^a
E	19	6
S0	36	15
S0a	4	1
Sa	27	13
Sab	22	7
Sb	52	39
Sbc	33	19
Sc	39	28
Scd	30	26
Sd	19	13
Sm-Im-BCD	39	23

Notes: ^a the galaxies analysed in this work have photometric data in all the following bands: *FUV* and *NUV* from GALEX, *gri* from SDSS, *JHK* from 2MASS, 11 and 22 μm from WISE, 100 and 160 μm from PACS and 250, 350, 500 μm from SPIRE, as well as $H\alpha$ imaging data and Balmer absorption lines from integrated spectroscopy.

detected in all the following photometric bands: *FUV* and *NUV* (GALEX), *gri* (SDSS), *JHK* (2MASS), 11 and 22 μm (WISE), 100 and 160 μm (PACS) and 250, 350, 500 μm (SPIRE), and have $H\alpha$ imaging data and Balmer absorption line indices from integrated spectroscopy. Systematic effects due to different sensitivities in the various bands should thus be minimal.

3.1. Photometry

An accurate determination of the physical properties of galaxies through an SED modelling technique requires a full sampling of the electromagnetic spectrum from the UV bands (recent star formation activity) to the near- (bulk of the stellar mass), mid- (dust attenuation), and far-infrared (dust mass) (e.g. Boselli 2011). The HRS has been covered at all wavelengths for this purpose. Ultraviolet data in the *FUV* (λ 1539 Å) and *NUV* (λ 2316 Å) have been collected thanks to two dedicated GALEX surveys (Boselli et al. 2011; Cortese et al. 2012b). Optical data in the *gri* bands have been extracted from the SDSS (Cortese et al. 2012b), while near-IR *JHK* data from 2MASS (Skrutskie et al. 2006). Mid-IR data are available thanks to the WISE (11 and 22 μm) and *Spitzer* (IRAC 8 μm) space missions (Ciesla et al. 2014). The sample has been also observed in the far-IR with PACS (100-160 μm ; Cortese et al. 2014) and SPIRE (250-350-500 μm ; Ciesla et al. 2012) on *Herschel*, while MIPS-*Spitzer* data (at 24 and 70 μm) are available only for a fraction of the sample (Bendo et al. 2012). Narrow band $H\alpha$ + $[NII]$ imaging data are available for the vast majority of the star forming galaxies of the sample (Boselli et al. 2015). The uncertainty in the different photometric bands slightly changes from galaxy to galaxy as shown in the original papers where the data are published. Typical uncertainties are given in Table 2.

3.2. Spectroscopy

Age-sensitive absorption Balmer line indices have been extracted from the integrated medium resolution ($R \simeq 1000$) spectra of the star forming (Boselli et al. 2013) and quiescent (Gavazzi et al. 2004) galaxies of the HRS. These spectra, which cover the 3500-7000 Å spectral domain, have been obtained by drifting the slit of the spectrograph over the disc of galaxies.

Table 2. Uncertainties in the different photometric and spectroscopic bands.

Band	Instrument	Uncertainty	ref
<i>FUV</i>	GALEX	15%	1
<i>NUV</i>	GALEX	15%	1
<i>g</i>	SDSS	15%	1
<i>r</i>	SDSS	15%	1
<i>i</i>	SDSS	15%	1
<i>J</i>	2MASS	15%	2
<i>H</i>	2MASS	15%	2
<i>K</i>	2MASS	15%	2
$8\mu\text{m}^a$	IRAC/Spitzer	15%	3
$11\mu\text{m}$	WISE	6%	3
$22\mu\text{m}$	WISE	13%	3
$24\mu\text{m}^a$	MIPS/Spitzer	4%	4
$70\mu\text{m}^a$	MIPS/Spitzer	10%	4
$100\mu\text{m}$	PACS/Herschel	16%	5
$160\mu\text{m}$	PACS/Herschel	12%	5
$250\mu\text{m}$	SPIRE/Herschel	6%	6
$350\mu\text{m}$	SPIRE/Herschel	8%	6
$500\mu\text{m}$	SPIRE/Herschel	11%	6
$\text{H}\alpha$	SPM	15%	7
$\text{H}\beta$	OHP	15%	8
$\text{H}\gamma$	OHP	15%	8
$\text{H}\delta$	OHP	15%	8

Notes: *a* available only for a fraction of the analysed galaxies.

References: 1) Cortese et al. (2012b), 2) Jarrett et al. (2003), 3) Ciesla et al. (2014), 4) Bendo et al. (2012), 5) Cortese et al. (2014), 6) Ciesla et al. (2012), 7) Boselli et al. (2015), 8) Boselli et al. (2013).

These spectra are thus representative of the whole galaxies and can be combined in the SED fitting analysis with the photometric data without any aperture correction. To remove the contribution of emission lines, the reduced spectra are fitted using the GANDALF code (Sarzi et al. 2006; Falcon-Barroso et al. 2006) as described in Boselli et al. (2015). This code has been designed to simultaneously fit the emission and absorption lines to properly separate the relative contribution of the stellar continuum from the nebular emission in the spectra of galaxies. Once removed the contribution of the emission lines, the stellar continuum spectra are normalised² to match the total emission of galaxies using the monochromatic *g*-band flux density of Cortese et al. (2012b) by convolving the spectrum with the SDSS *g*-band filter transmissivity.

3.3. Corollary data

The activity of star formation in galaxies is tightly connected to their total gas content (Boselli et al. 2001). The interaction of galaxies with the hostile cluster environment removes the gaseous component inducing a quenching of the star formation activity. We thus compare the star formation properties of the sample galaxies to their amount of gas. Atomic and molecular gas data for the large majority of the sample have been collected and homogenised in Boselli et al. (2014a). Atomic gas masses are used to derive the HI-deficiency parameter *HI-def* defined as the difference in logarithmic scale between the expected and the observed HI mass of a galaxy of given angular size

² Because of the drifting observing technique, the spectra do not give absolute fluxes.

and morphological type (Haynes & Giovanelli 1984). The HI-deficiency for all the HRS galaxies given in Boselli et al. (2014a) has been determined using the recent calibration of Boselli & Gavazzi (2009).

HI data are also important for measuring the rotational velocity of the target galaxies, an essential parameter in the following analysis (see sect. 4).

4. The SED modelling

4.1. The models

The observed SED of the HRS galaxies are fitted using the CIGALE³ SED modelling code (Noll et al. 2009; Ciesla et al. 2016; Boquien et al. in prep.). Its application to the HRS galaxies has been already described in detail in Ciesla et al. (2014, 2016). Here we just summarise the main properties of this code. CIGALE produces synthetic UV to far infrared SED of galaxies using different stellar population synthesis models available in the literature to trace the stellar emission and different dust models or empirical templates to trace the dust emission. The stellar and dust emissions are related by the dust attenuation which is estimated taking into account an energetic balance between the energy emitted by the different stellar populations absorbed by dust and re-emitted in the infrared. The model spectra are constructed assuming different star formation histories, metallicities, and attenuation laws (see below). They are then compared to the multifrequency observations once convolved with the transmissivity profile of different photometric bands generally used in ground-based and space missions. The code identifies the best fitted model through a χ^2 minimisation and makes a probability distribution function (PDF) analysis to identify the likelihood-weighted mean value and standard deviation for different physical parameters such as the stellar mass, the star formation rate, etc. This code has been successfully used to reconstruct the star formation history of high-*z* and local galaxies (Buat et al. 2014, Boquien et al. 2016, Lo Faro et al. in prep.), including those of the HRS (Boquien et al. 2012, 2013; Ciesla et al. 2014, 2016).

The novelty introduced in this work is the inclusion in the fitted variables of widely used age-sensitive spectral features extracted from medium resolution ($R \sim 1000$) spectra. For this purpose we use the high resolution version of the Bruzual & Charlot population synthesis models (Bruzual & Charlot 2003). Consistently with our previous works, the far infrared part of the spectrum is fitted with an updated version of the Draine & Li (2007) physical models of dust emission. These models are characterised by different variables tracing the dust properties: q_{PAH} , the fraction of the total dust mass in PAHs containing less than 10^3 C atoms, U_{min} , the intensity of the diffuse interstellar radiation field, and γ , the fraction of dust heated by young stars within photodissociation regions (PDRs), as extensively described in Draine & Li (2007) and Draine et al. (2007).

4.2. Parametrisation of the star formation history

Several observational properties of local galaxies, including SED, colour and metallicity gradients, and different scaling relations, are well reproduced assuming that galaxies are coeval

³ <http://cigale.lam.fr/>

Table 3. Coefficients of the parametric star formation history.

Velocity km s ⁻¹	a	b	c
40	4.73	-0.11	0.79
50	5.28	0.03	0.68
60	5.77	0.16	0.57
70	6.21	0.29	0.47
80	6.62	0.41	0.36
90	6.99	0.51	0.27
100	7.34	0.61	0.18
150	8.74	0.98	-0.20
220	10.01	1.25	-0.55
290	10.82	1.36	-0.74
360	11.35	1.37	-0.85

systems and evolved following a delayed star formation history (Sandage 1986; Boissier & Prantzos 2000; Boselli et al. 2001; Gavazzi et al. 2002b). Different delayed star formation histories have been proposed in the literature. In this work we adopt that derived by Buat et al. (2008) to reproduce the star formation history of the multizone chemo-spectrophotometric models of galaxy evolution of Boissier & Prantzos (2000). These models have been successful in reproducing the colour, metallicity and gas radial profiles of nearby galaxies such as those analysed in this work and their typical scaling relations at different redshift (e.g. Boissier & Prantzos 2000, 2001; Boissier et al. 2001, 2003; Munoz-Mateos et al. 2007, 2009, 2011). This star formation history is parametrised with a polynomial of the form:

$$\log SFR(t)_{secular} = a + b \log t + ct^{0.5} \quad (1)$$

where t is the time ellapsing after the first generation of stars are formed and the coefficients a , b , and c for different rotational velocities are given in Table 3, the rotational velocity being the free parameter. A finer grid of a , b , and c coefficients has been determined by interpolating the values given in Table 3 in the velocity range 40-360 km s⁻¹.

Following this star formation history, in massive galaxies the bulk of the stars are formed at early epochs, while in dwarf systems the star formation activity is still rising. This parametrisation has been preferred to other analytical forms because its main parameter regulating the secular evolution of galaxies, the rotational velocity, is an observable available for the sample galaxies. This observable is crucial for constraining the secular evolution of the target galaxies independently from the spectrophotometric data, and thus its use reduces any possible degeneracy in the determination of the present star formation rate, quenching age and quenching factor of the target galaxies. To check whether this assumption does not introduce any systematic bias in the results, in Appendix A we perform the same analysis presented in this and in the following sections also leaving the rotational velocity as a free parameter, and we show that our results are reliable. The rotational velocity is derived from the HI line width WHI measured using single dish observations and reported in Boselli et al. (2014a) through the relation:

$$vel_{rot} = \frac{WHI}{2 \times \sin(incl)} \quad (2)$$

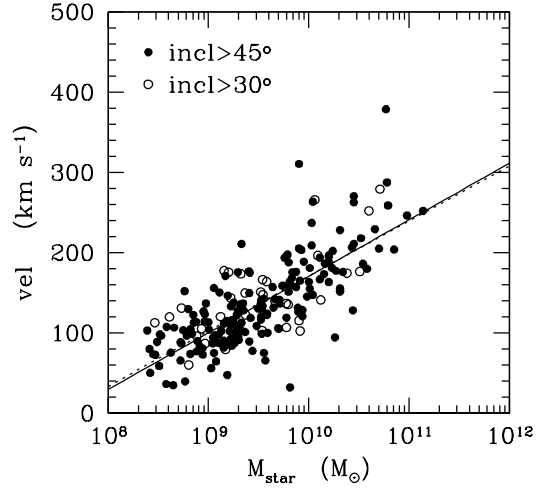


Fig. 1. The rotational velocity vs. stellar mass relation derived for HRS galaxies with an inclination $incl > 45^\circ$ (filled dots) and $incl > 30^\circ$ (filled and empty dots). The solid and dotted lines indicate the linear best fit to the data for galaxies with $incl > 45^\circ$ and $incl > 30^\circ$, respectively.

where $incl$ is the inclination of the galaxy⁴. For galaxies with an inclination $incl \leq 30^\circ$, or galaxies without HI data, the rotational velocity is derived using the stellar mass Tully-Fisher relation⁵ determined for the late-type galaxies of the HRS using the set of data given in Boselli et al. (2014a) (see Fig. 1). This relation is (linear fit):

$$vel_{rot} [\text{km s}^{-1}] = 68.71 \pm 4.17 \times \log M_{star} [M_\odot] - 516.11 \pm 39.68 \quad (\rho = 0.75) \quad (3)$$

(where ρ is the correlation coefficient), has been derived using 217 galaxies of the sample with available data⁶. For the early-type galaxies of the sample, the rotational velocity is tentatively derived from the same stellar mass-rotational velocity relation derived for late-type galaxies (den Heijer et al. 2015). Although early-type systems do not follow the same scaling relations than spirals, this assumption is justified by the fact that we want to test whether these typical cluster objects have been formed through the transformation of star forming systems after a gas stripping phenomenon.

To reproduce the quenching of the star formation activity of the Virgo cluster galaxies we use a formalism similar to the one proposed in Ciesla et al. (2016), i.e. we apply an instantaneous

⁴ The factor 2 takes into account the fact that WHI is the total (receding plus approaching) HI line width.

⁵ The stellar mass relation has been preferred to the baryonic Tully-Fisher relation just because molecular gas masses are not available for the low mass galaxies of the sample.

⁶ The relation does not change significantly if the fit is restricted to a smaller sample of galaxies with $incl > 45^\circ$.

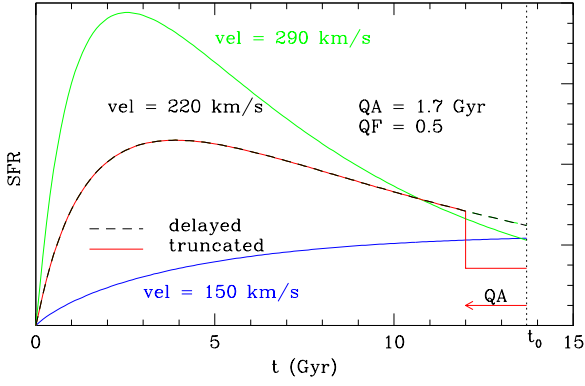


Fig. 2. The parametric star formation history used in this work for a galaxy with a rotational velocity of 220 km s^{-1} (black dashed line), 290 km s^{-1} (green solid line) and 150 km s^{-1} (blue solid line). The black dashed line shows the delayed star formation history given in eq. (1), the red solid line the truncated one (eq. 4) for the case $vel = 220 \text{ km s}^{-1}$ (adapted from Ciesla et al. 2016).

truncation of the star formation history parametrised by the expression:

$$SFR(t) = \begin{cases} SFR(t)_{secular} & \text{if } t_0 - t \geq QA \\ (1 - QF) \times SFR(t_0 - QA)_{secular} & \text{if } t_0 - t < QA \end{cases} \quad (4)$$

where $SFR(t)_{secular}$ is the star formation rate expected for a secular evolution (eq. 1), QA is the quenching age, QF the quenching factor and t_0 the age of the universe at the present epoch, as depicted in Fig. 2. This is obviously a crude representation of the physical process affecting galaxies. It is indeed known from observations and simulations that the gas stripping process is not instantaneous, but rather requires a certain time to be efficient. Furthermore the duration of the stripping process strongly depends on the perturbing mechanism: it is very long (several Gyrs) for starvation (Boselli et al. 2006) and harassment (Moore et al. 1998), where multiple flyby encounters of cluster galaxies are required, while it is relatively short for ram pressure. We prefer, however, this simple representation to a more physically motivated parametrisation such as the one proposed in Wetzel et al. (2013) because we want to reduce the number of free parameters and thus limit any possible degeneracy in the derived quantities.

Hydrodynamical simulations consistently indicate that the total amount of gas of typical cluster galaxies is removed by ram pressure in $\lesssim 1.5 \text{ Gyr}$ (Roediger & Bruggen 2007; Tonnesen & Bryan 2009). Observations and simulations, however, also indicate that most of the gaseous component is removed on much shorter timescales because the ram pressure stripping efficiency, which scales as ρV^2 (Gunn & Gott 1972, where ρ is the density of the ICM and V the velocity of galaxies within the cluster), is at its maximum only when the galaxy is crossing the core of the cluster. This is well depicted in Figure 3 of Vollmer et al. (2001) which indicates that the efficiency of ram pressure increases by a factor of ≈ 10 on timescales $\lesssim 100 \text{ Myr}$. These timescales for gas stripping and quenching of the star formation activity of Virgo cluster galaxies are comparable to those derived with independent techniques on a dozen of well known Virgo cluster galaxies (see sect. 5).

The parametrisation given in eq. 4 to reproduce the truncation of the star formation activity of cluster galaxies is, however, extreme. To test how much the results obtained in the following analysis depend on this assumption we also use as other extreme case a smooth constantly declining star formation history (see Appendix A). The main results of the analysis do not change significantly.

4.3. Spectral line indices

To constrain the typical age of truncation of the star formation activity of the perturbed cluster galaxies we add several age-sensitive spectral indices. To be used and weighted as the other broad photometric bands in the CIGALE SED fitting code, these spectral indices must be defined as photometric bands. The most widely used age-sensitive spectral indices present in the visible spectra of galaxies are the Balmer absorption lines ($H\beta$, $H\gamma$, $H\delta$) and the D_{4000} (Worthey 1994; Poggianti & Barbaro 1997; Balogh et al. 1999; Kauffmann et al. 2003; Brinchmann et al. 2004). In the standard Lick/IDS system, the Balmer indices are defined as equivalent widths. They cannot be directly used in CIGALE. We thus defined some pseudo filters centered on the Balmer lines where the transmissivity is set positive on the stellar continuum on the wedges of the absorption line and negative on the absorption line, as depicted in Fig. 3. The integral of the transmissivity on the blue and red stellar continua is set equal to that over the absorption line index, so that for flat spectra the total flux within these pseudo filters is zero:

$$\int_{blue_1}^{blue_2} T(\lambda) d\lambda + \int_{red_1}^{red_2} T(\lambda) d\lambda = - \int_{line_1}^{line_2} T(\lambda) d\lambda \quad (5)$$

and

$$\int_{line_1}^{line_2} T(\lambda) d\lambda = 1 \quad (6)$$

for the normalisation of the filter transmissivity, where $blue_1$ and $blue_2$ and red_1 and red_2 stand for the limits at shorter and longer wavelengths where the continuum in the Lick/IDS indices is measured, while $line_1$ and $line_2$ the interval in wavelengths for the absorption line⁷. The first condition is required to make the contribution of the stellar continuum on the on and off bands the same. To be as consistent as possible with the Lick/IDS definition, the continuum and the line emission are measured on the same intervals as in Worthey & Ottaviani (1997) and Worthey (1994) (wide filter definition, see Table 4).

The D_{4000} spectral index generally used in the literature (e.g. Balogh et al. 1999) is defined as a ratio of the flux measured in two spectral ranges at shorter and longer wavelengths than the spectral discontinuity. Being defined as a flux ratio, this index cannot be simulated with a similarly defined pseudo filter and thus it will not be used in this analysis.

The $H\alpha$ emission, which is due to the emission of the gas of the ISM ionised by the UV photons produced in O and early-B massive stars ($\gtrsim 10 M_{\odot}$; Kennicutt 1998b; Boselli et al. 2009), is sensitive to much younger stellar populations ($\approx 5 \text{ Myr}$; Fig. 4). Population synthesis models provide the number of ionising photons N_{ν} for a given star formation history. We thus use the $H\alpha$

⁷ The transmissivity of the filter is set negative on the absorption line just because the CIGALE fitting code requires positive values in the different bands.

luminosities derived from narrow band imaging data to estimate the number of ionising photons using the relation (Osterbrock & Ferland 2006):

$$N_v = \frac{L(H\alpha) [\text{erg s}^{-1}]}{1.363 \times 10^{-12}} \quad (7)$$

where $L(H\alpha)$ is the $H\alpha$ luminosity. Narrow band $H\alpha$ + $[NII]$ imaging data are first corrected for $[NII]$ contamination using the long slit spectroscopy of Boselli et al. (2013) (using the updated table given in Boselli et al. 2015). We then make the hypothesis that all the ionising radiation ($\lambda < 912 \text{ \AA}$) is absorbed by the gas, or in other words that the escape fraction is zero and that the ionising photons do not contribute to the heating of dust ($f=1$). Narrow band $H\alpha$ + $[NII]$ imaging data are also corrected for dust attenuation. This is done using the Balmer decrement whenever possible, otherwise using standard recipes based on monochromatic $22 \mu\text{m}$ WISE data as described in Boselli et al. (2015). CIGALE requires flux densities measured within a filter band-pass. For this reason we defined another pseudo filter (L_{yC}) to characterise the ionising radiation with a positive and constant transmissivity for $\lambda < 912 \text{ \AA}$:

$$\int_0^{912\text{\AA}} T(\lambda)d\lambda = 1 \quad (8)$$

Since CIGALE requires a flux density in this photometric band, the number of ionising photons must be transformed into mJy. This is done using a calibration that we derived on the mock catalogue (see sect. 4.4) by measuring on the spectral energy distribution of the simulated galaxies the flux density within this pseudo filter and comparing it to the number of ionising photons given by the population synthesis models:

$$L_{yC} [\text{mJy}] = \frac{1.07 \times 10^{-37} \times L(H\alpha) [\text{erg s}^{-1}]}{D^2 [\text{Mpc}]} \quad (9)$$

or equivalently:

$$L_{yC} [\text{mJy}] = 1.079 \times 10^4 \frac{SFR_{Salp} [M_{\odot}\text{yr}^{-1}]}{D^2 [\text{Mpc}]} \quad (10)$$

Figure 4 shows how the flux within these newly defined pseudo filters and in the GALEX FUV and NUV age-sensitive photometric bands changes when the star formation activity of a typical star forming model galaxy with parameters given in Table 5 is abruptly truncated. The Balmer absorption line indices are sensitive to stellar populations of intermediate ages and are thus indicated to characterise the quenching age for truncations ≈ 500 Myr old. The FUV and NUV flux densities are sensitive to relatively younger ages (≈ 100 - 200 Myr), while the number of Lyman continuum photons derived from $H\alpha$ imaging data to much younger stellar populations ($\lesssim 5$ Myr; Boquien et al. 2014). The determination of the uncertainty on the flux in the pseudo filters is made difficult by several factors (uncertainty on the normalisation, noise in the stellar continuum, electronic noise in the spectrum). Similarly, the uncertainty on the number of ionised photons derived from narrow band $H\alpha$ imaging data is hardly quantifiable because of the different steps required to transform observables ($H\alpha$ + $[NII]$ fluxes) with their own uncertainties to physical quantities ($[NII]$ contamination, dust attenuation correction...). There are also large uncertainties in the stellar population synthesis models on the intensity of the Lyman continuum photons (Levesque et al. 2012). We thus assume a conservative uncertainty of 15% in all the pseudo filters, but recall

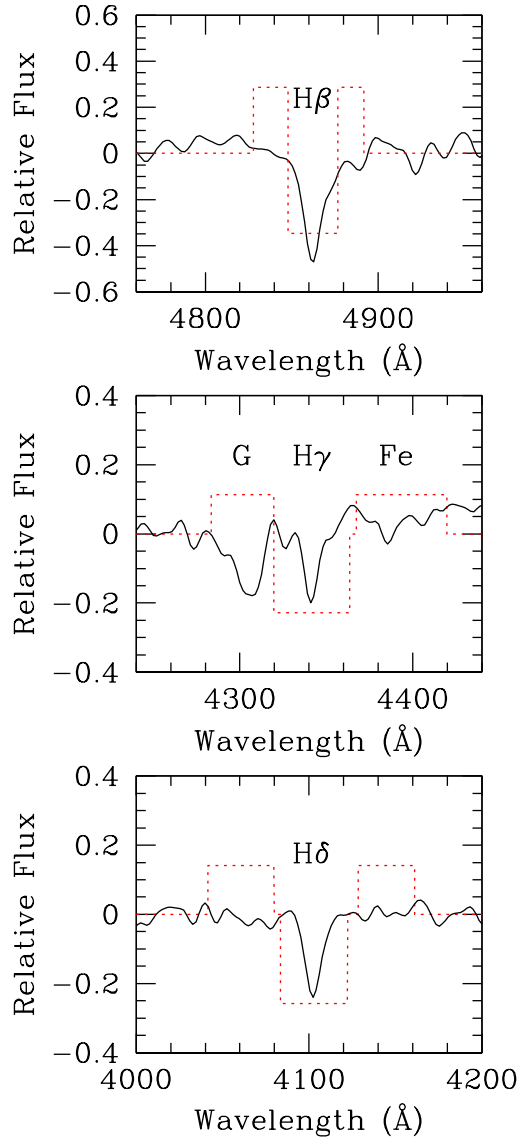


Fig. 3. The transmissivity of the newly defined pseudo filters (red dotted line) centered on the age-sensitive $H\beta$, $H\gamma$, and $H\delta$ lines is plotted as a function of wavelength and compared to the integrated spectrum of NGC 4569 once the emission lines are removed (black solid line; Boselli et al. 2013).

Table 4. Pseudo filters definitions.

Filter	$blue_1 - blue_2$	$line_1 - line_2$	$red_1 - red_2$
$H\beta$	4827.875-4847.875	4847.875-4876.625	4876.625-4891.625
$H\gamma$	4283.50-4319.75	4319.75-4363.50	4367.25-4419.75
$H\delta$	4041.60-4079.75	4083.50-4122.25	4128.50-4161.00

that the CIGALE code adds a 10% uncertainty as in all other bands. The same statistical weight is applied to all photometric bands in the fitting procedure (including the newly defined pseudofilters)

Figure 5 gives the rotational velocity distribution for the late-type galaxies of the sample, and indicates that the critical parameters necessary for constraining the recent star formation activity (the pseudo filter bands as well as the FUV and NUV bands) are

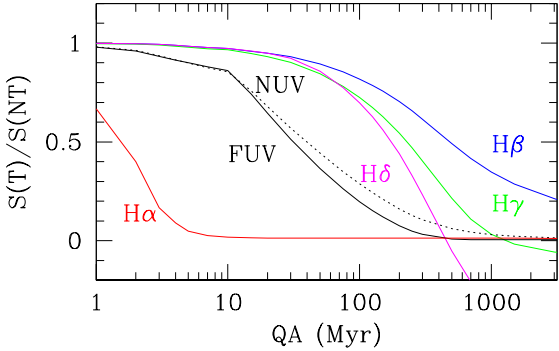


Fig. 4. The expected variation of the flux density $S(T)$ for a truncated star formation history in the *FUV* and *NUV* bands and in the newly defined LyC ($H\alpha$), $H\beta$, $H\gamma$, and $H\delta$ pseudo filters after a total quenching of the star formation activity (quenching factor $QF = 1$) with respect to that of an unperturbed galaxy ($S(NT)$) as a function of the quenching age QA for a model galaxy with properties given in Table 5.

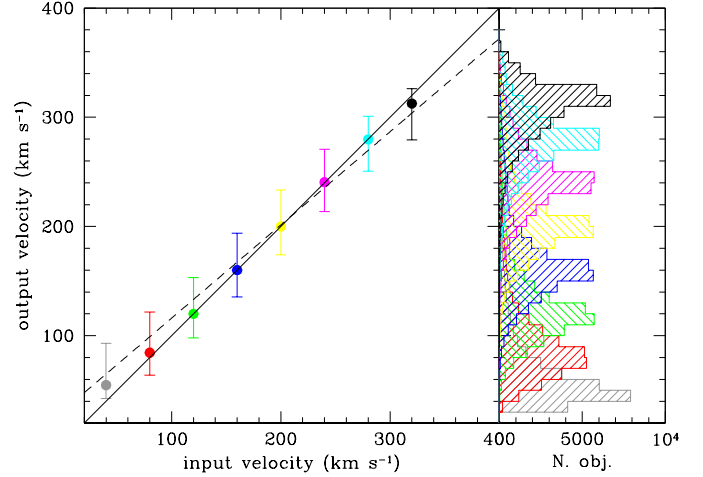


Fig. 6. Relationship between the input rotational velocity of the simulated galaxies and the output velocity derived from the PDF analysis of the mock SED (left panel). Dots are median values while error bars are the 16% and 84% quartiles of the distribution. The solid line shows the 1:1 relationship, while the dashed line the linear best fit to the data. The right panel shows the distribution of output velocities derived from the PDF analysis for a given value of the input velocity for the simulated galaxies.

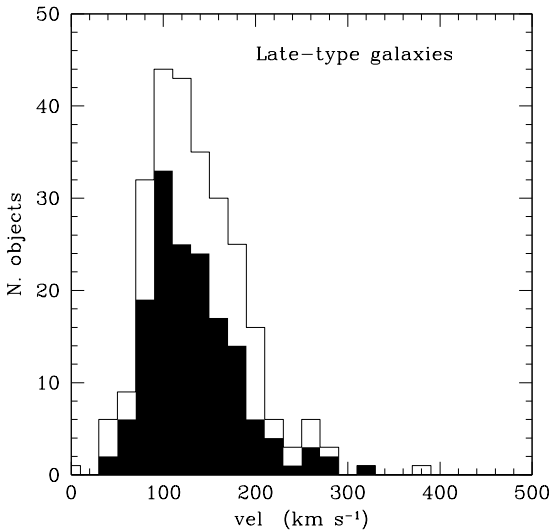


Fig. 5. Distribution of the rotational velocity of all the late-type galaxies of the sample (empty histogram) and of those objects with data in the newly defined pseudo filter bands.

available for most of them. It also shows that the range in rotational velocity of the HRS galaxies is within the one covered by the star formation history given in eq. 1 and in Table 3.

4.4. Mock catalogue of simulated galaxies

To test the solidity of this approach, we first generate a grid of simulated galaxies and extract their SED in the same photometric and spectroscopic bands analysed in this work by varying different input parameters in the CIGALE code, as listed in Table 5. These different parameters have been chosen to sample in a relatively uniform way the expected parameter space for the HRS galaxies in terms of star formation history, dust attenuation and dust properties. Since the most critical parameters for the following analysis are the present day star formation rate, the star formation history, the quenching factor and the quenching age of the perturbed galaxies, these parameters have been sampled in narrower bins than the other variables in the simulated galaxies. The resulting catalogue of simulated SED includes 282528 objects.

We then produced a mock catalogue by artificially introducing noise in the simulated SED according to the typical error in the different photometric bands. We then fitted this simulated mock catalogue of SED and made a PDF analysis of the most critical variables. To avoid edge effects in the PDF analysis, we analysed a wider range in the parameter space than in the one used to construct the SEDs. This has been done only for those variables analysed in this work, i.e. the quenching factor and the quenching age, as described in Table 5. Given the physical limit of the two variables (the quenching age must be ≥ 0 and the quenching factor cannot be > 1), the PDF cannot be sampled symmetrically. We also sampled negative quenching factors which might be representative of a recent burst of star formation (see Table 5).

Figures 6, 7, and 8 show the relationship between the input parameters used to define the star formation history of the simulated galaxies and the distribution of output parameters derived from SED fitting of the mock catalogue. The analysis of these Figures reveals that:

Table 5. Input parameters used to create the mock catalogue as defined in sec. 4.1.

Parameter	value	Units
Pop.Synth.Mod.	Bruzual & Charlot (2003)	
Dust model	Draine & Li (2007)	
IMF	Salpeter	
Metallicity	0.02	
Velocity	40, 80, 120, 160, 200 , 240, 280, 320, 360	km s ⁻¹
QF	-0.4, -0.2, 0, 0.2, 0.4, 0.6, 0.7, 0.8, 0.9, 0.95, 1	
QA	0, 5, 10, 20, 50, 100, 150, 200, 250, 300, 500, 700, 1000, 1500	Myr
$E(B - V)_{young}$	0.05, 0.1, 0.2, 0.4	
$E(B - V)_{old}$	0.44	
Q_{PAH}	0.47, 2.50, 4.58 , 6.63	
U_{min}	0.1, 0.5, 2.0 , 4.0, 8.0, 20	
α	2.5	
γ	0.01, 0.03 , 0.1	

Note: The parameters for the model galaxy used to trace the variation of the flux densities in the pseudo filters after a total quenching of the star formation activity shown in Fig. 4 are given in boldface.

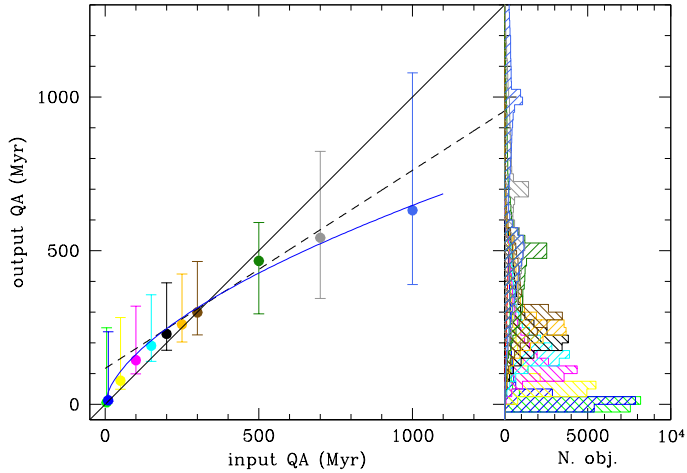


Fig. 7. Relationship between the input quenching age of the simulated galaxies and the output quenching age derived from the PDF analysis of the mock SED (left panel). Dots are median values while error bars are the 16% and 84% quartiles of the distribution. The solid line shows the 1:1 relationship, while the dashed line the linear best fit to the data, the blue solid line a second degree polynomial fit. The right panel shows the distribution of output quenching ages derived from the PDF analysis for a given value of the input quenching age for the simulated galaxies.

1) The rotational velocity, which is the parameter regulating the secular evolution of galaxies and thus their long term star formation history, is well measured in the PDF analysis of the mock catalogue.

2) The quenching age extracted from the PDF analysis matches quite well the input values for quenching ages $\lesssim 500$ Myr, while it systematically underestimates the input value for older

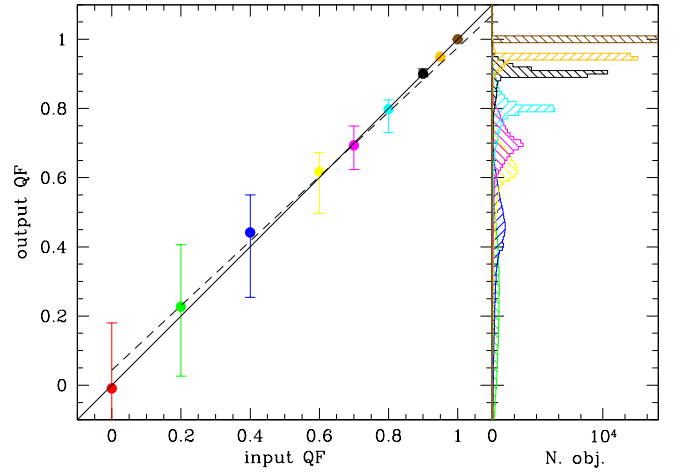


Fig. 8. Relationship between the input quenching factor of the simulated galaxies and the output quenching factor derived from the PDF analysis of the mock SED (left panel). Dots are median values while error bars are the 16% and 84% quartiles of the distribution. The solid line shows the 1:1 relationship, while the dashed line the linear best fit to the data. The right panel shows the distribution of output quenching factor derived from the PDF analysis for a given value of the input quenching factor for the simulated galaxies.

quenching ages (by \sim a factor of 2 for a quenching age of 1 Gyr). The uncertainty on the derived parameter increases with increasing input quenching ages.

3) The quenching factor extracted from the PDF analysis is tightly connected to the input value. The uncertainty on its measure, however, increases with decreasing quenching factor.

Point 2) and 3) can be understood if we consider that whenever the truncation occurred at early epochs (large QA) and/or the

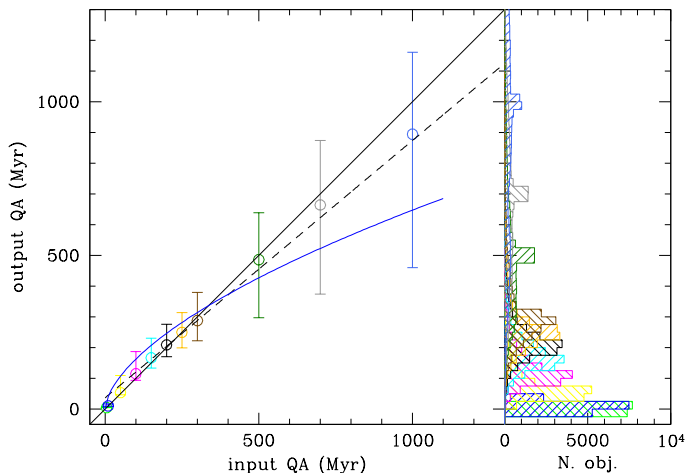


Fig. 9. Relationship between the input quenching age of the simulated galaxies and the output quenching age derived from the PDF analysis of the mock SED restricted to galaxies with an input quenching factor $QF > 0.5$ (left panel). Dots are median values while error bars are the 16% and 84% quartiles of the distribution. The solid line shows the 1:1 relationship, while the dashed line the linear best fit to the data, the blue solid line a polynomial fit derived for the whole mock sample shown in Fig. 8. The right panel shows the distribution of output quenching ages derived from the PDF analysis for a given value of the input quenching age for the simulated galaxies.

quenching factor is small, the imprints of these effects on the SED are hardly distinguishable from those due to possible variations in the secular evolution of galaxies. Indeed, if we limit for instance the comparison of the input quenching age of the simulated galaxies and the output quenching age derived from the PDF analysis of the mock SED to those galaxies with $QF > 0.5$, thus to those objects where the truncation of the star formation activity is significant, we obtain significantly better results (see Fig. 9).

We already analysed the reliability of using a SED fitting analysis to study short term variations in the star formation activity of perturbed galaxies in Ciesla et al. (2016). The results of our analysis are directly comparable since based on the same sample of galaxies and on the same set of photometric data. Ciesla et al. (2016) have shown that, whenever UV data are available, the SED fitting analysis gives a reliable estimate of the quenching factor, but fails to estimate the quenching age and τ_{main} , the typical timescale characterising the secular evolution of galaxies. As discussed in Ciesla et al. (2016), this is probably due to a degeneracy between the free parameters characterising the parametrised star formation history. To overcome this problem and capitalise on the promising results obtained in Ciesla et al. (2016) we adopt here a different star formation history where the secular evolution of galaxies is not a free parameter as in Ciesla et al. (2016; the τ_{main} parameter) but rather it is observationally constrained from the rotational velocity of the galaxy as derived from HI data (see sec. 4.2).

The number of free parameters necessary to parametrise the star formation history is thus reduced from three to two. At the same time we use a significantly larger number of age sensitive photometric bands (LyC, *FUV*, *NUV*, H β , H γ , H δ) than in Ciesla et al. (2016) (*FUV*, *NUV*). In particular, the introduction of the number of ionising photons derived from the H α emission, which are produced in young ($\lesssim 10^7$ yr) and massive ($M \gtrsim 10 M_{\odot}$) stars, is critical for constraining recent episodes of star formation. These improvements reduce the degeneracy between the fitted parameters and have a significant impact on the reliability of their determination. The comparison of Figures 7 and 8 with Figures 4 and 5 of Ciesla et al. (2016), indeed, indicates a remarkable increase in the accuracy in the quenching parameters derived in the present work.

5. SED fitting of representative galaxies

A further test in the reliability of the output parameters of our SED fitting code can be done by comparing them to those derived with independent techniques on a few well known galaxies of the sample. A dozen of Virgo cluster galaxies of the HRS, indeed, have been studied in great detail using a combination of spectro-photometric and kinematic data with models tuned to reproduce the interaction of galaxies with the hostile cluster environment.

5.1. NGC 4569

We first test the reliability of our fitting procedure using NGC 4569, the brightest late-type galaxy of the Virgo cluster. This galaxy is undergoing a ram pressure stripping event as revealed by a dynamically perturbed velocity field of the gaseous component (Vollmer et al. 2004), a truncated gaseous and stellar disc in the young stellar populations (H α , *FUV*, *NUV*), while a normal extended disc in the old stellar populations (Boselli et al. 2006), and a ~ 100 kpc extended tail of ionised gas formed during the interaction with the hot and dense intracluster medium (Boselli et al. 2016). The dynamical models of Vollmer et al. (2004) indicate that the gas stripping process took place ~ 300 Myr ago. Using tuned models of galaxy evolution especially tailored to take into account the effects of ram pressure stripping, Boselli et al. (2006) were able to reproduce the observed radial truncation in the gaseous disc and in the stellar disc at different wavelengths if the peak of the stripping process occurred ~ 100 Myr ago. By studying the stellar population properties of the outer disc of NGC 4569 using IFU spectroscopic data, Crowl & Kenney (2008) concluded that the star formation activity of NGC 4569 ended outside the truncation disc ~ 300 Myr ago. We thus have consistent and independent indications that this galaxy was perturbed recently (100-300 Myr). The models of Boselli et al. (2006) also indicate that the activity of star formation of this galaxy was reduced by 95% ($QF = 0.95$).

The observed UV to FIR SED of NGC 4569 is well reproduced by CIGALE using a truncated star formation history, while the fit does not match the photometric data in the UV to NIR bands if a simple delayed star formation history is adopted (Fig. 10). The match between the best model and the observations is evident also at high resolution in the optical domain, where the truncated model can be directly compared to the normalised observed spectrum (Fig. 11). Despite a systematic shift in the model vs. observations already present in the UV to FIR SED in the *g* band used for the normalisation of the integrated spectrum, there is a very good agreement in the high resolution

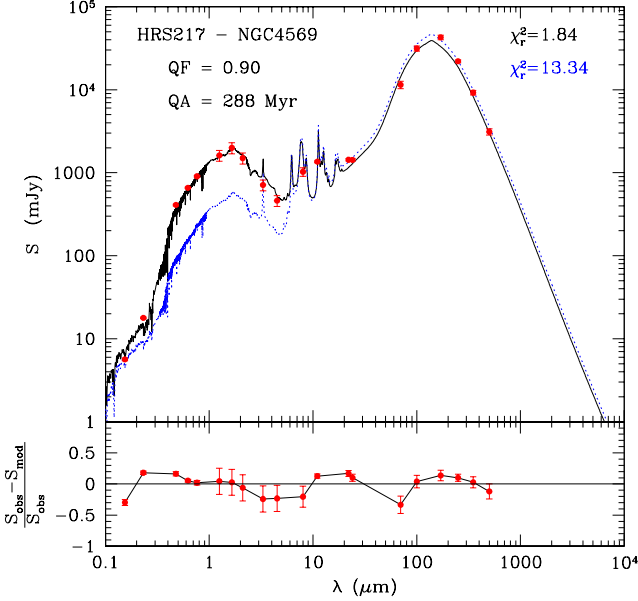


Fig. 10. The observed UV to FIR SED of NGC 4569 (HRS 217) (red filled dots) is compared to the best fitted model derived by CIGALE using a truncated star formation history (black solid line) or a normal delayed star formation history (blue dotted line) (upper panel). The normalised difference between the observed and model value in the different photometric bands is plotted vs. lambda in the lower panel (for a truncated star formation history).

absorption features, and in particular in the age sensitive Balmer absorption lines used in the fit.

Our SED fitting code gives $QA = 288 \pm 23$ Myr and a $QF = 0.90 \pm 0.05$, values very consistent with those derived with independent techniques. NGC 4569 also belongs to the SINGS sample of galaxies (Kennicutt et al. 2003) and thus have an integrated spectrum taken by Moustakas et al. (2010). If we combine the photometric data to the spectroscopic dataset of Moustakas et al. (2010) we derive very similar values for the quenching age ($QA = 299 \pm 15$ Myr) and the quenching factor ($QF = 0.90 \pm 0.05$), indicating that the derived values are robust vs. the use of different spectroscopic datasets.

5.2. Other galaxies

The same comparison can be extended to a few other galaxies with estimates of the quenching age from dynamical models or from IFU spectroscopic data of the outer discs (see Fig. 12 and Table 6). We recall that the timescales derived using dynamical models indicate the epoch when the gaseous component started to be perturbed. This might not coincide with the beginning of the decrease of the star formation activity, which generally occurs after the gas has been stripped (Boselli et al. 2008a; Crowl & Kenney 2008). Furthermore, the analytical definition of the star formation history used in this work does not allow negative quenching ages as dynamical models do (the gas stripping process starts before the peak of the ram pressure stripping process has been reached). Despite the large uncertainty in the plotted parameters, overall there is a reasonable agreement between the quenching ages derived using different techniques when the

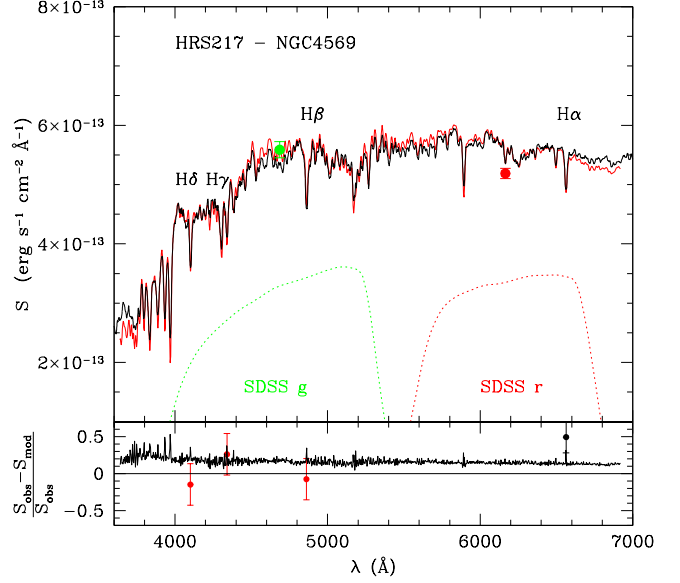


Fig. 11. The integrated spectrum of NGC 4569, with a resolution of $R \sim 1000$, corrected for line emission (red line), normalised to the flux density in the g band (green filled dot), is compared to the best fitted model derived by CIGALE using a truncated star formation history (black solid line; the model spectrum is shifted on the Y-axis by a factor of $+8 \times 10^{-14}$ to match the observed spectrum). The red filled dot shows the r -band photometric point, while the transmissivity of the SDSS g and r bands is traced by the green and red dotted curves (upper panel). The normalised difference between the two spectra is plotted vs. lambda in the lower panel. The red filled dots indicate the normalised difference between the values of the $H\beta$, $H\gamma$, and $H\delta$ pseudo filters and those measured on the best fitted model. The black filled dot at $\lambda = 6563$ Å shows the normalised difference between the observed Lyman continuum pseudo filter, derived from the extinction corrected $H\alpha$ image of the galaxy, and the Lyman continuum flux measured on the best fitted model.

comparison is limited to those objects with a good quality fit (reduced $\chi_r^2 \leq 3$).

6. SED fitting of the HRS

Since we want to focus our analysis on the quenching phenomenon, the model SED used in the following analysis are constructed using for each galaxy the appropriate rotational velocity as derived from kinematical data (or from the Tully-Fisher relation as explained in sect. 4.2 whenever the former is not available). The grid of parameters used to fit the observed data are given in Table 7.

Figure 13 shows the relationship between the flux densities in the four pseudo filters derived from the PDF analysis vs. the one measured on the observed spectra. The correlation between the two variable is excellent in the $H\beta$ and $H\delta$ bands, while the scatter increases in $H\gamma$ and particularly in the Lyman continuum derived from the $H\alpha$ data. The low scatter in the $H\beta$ and $H\delta$ relations is probably due to the fact that both variables are sensitive to stellar populations of young-to-intermediate age (see Fig. 4), already well constrained by the FUV-to-far-IR photometric

Table 6. Quenching parameters derived using other techniques for some HRS galaxies in the Virgo cluster.

HRS	NGC/IC	vel km s ⁻¹	QA Myr	QF	χ_r^2	age Myr	ref	method
(1)	(2)	(3)	(4)	(5)	(6)	(7)	(8)	(9)
102	4254	175	129 ± 478	-0.06 ± 0.36	3.14	280	8	dyn
124	4330	120	172 ± 50	0.89 ± 0.04	1.09	-100	3	dyn
124	4330	120	172 ± 50	0.89 ± 0.04	1.09	200-400	11	phot
144	4388	180	61 ± 25	0.74 ± 0.06	1.00	225±100	6	spec
144	4388	180	61 ± 25	0.74 ± 0.06	1.00	120	9	dyn
149	4402	120	1302± 320	0.90 ± 0.04	3.23	200 ^a	6	spec
156	4419	95	1610± 75	0.95 ± 0.05	6.15	500±150	6	spec
159	4424	32	501 ± 25	0.95 ± 0.05	2.81	275±75	6	spec
163	4438	130	576 ± 250	0.95 ± 0.05	3.66	100	4	dyn
172	IC3392	100	299 ± 15	1.0 ± 0.05	2.90	500±100	6	spec
190	4501	290	77 ± 135	0.81 ± 0.09	2.88	-250	7	dyn
197	4522	105	64 ± 101	0.80 ± 0.04	3.01	50	5	dyn
197	4522	105	64 ± 101	0.80 ± 0.04	3.01	100±50	6	spec
217	4569	220	288 ± 23	0.90 ± 0.05	1.84	100	1	model
217	4569	220	288 ± 23	0.90 ± 0.05	1.84	300	2	dyn
217	4569	220	288 ± 23	0.90 ± 0.05	1.84	300±50	6	spec
221	4580	105	646 ± 101	0.95 ± 0.05	1.52	475±100	6	spec
247	4654	175	645 ± 804	0.40 ± 0.21	2.39	500 ^a	10	dyn

Column 1: HRS name; Column 2: NGC/IC name; Column 3: rotational velocity used in the CIGALE fit; Column 4: QA and error derived using CIGALE; Column 5: QF and error derived using CIGALE; Column 6: reduced χ_r^2 ; Column 7: age of the interaction derived in the literature; Column 8: References: 1: Boselli et al. (2006); 2: Vollmer et al. (2004); 3: Vollmer et al. (2012); 4: Vollmer et al. (2009); 5: Vollmer et al. (2006); 6: Crowl & Kenney (2008); 7: Vollmer et al. (2008a); 8: Vollmer et al. (2005); 9: Vollmer & Huchtmeier (2003); 10: Vollmer (2003); 11: Abramson et al. (2011); Column 8: method used to derive the age of the interaction: *dyn* stands for dynamical models based on the HI and/or CO data; *spec* for IFU spectroscopy of the outer stellar disc; *model* for multizone-chemospectrophotometric models of galaxy evolution; *phot* derived using UV-to-optical photometry.

Notes: a = upper limit.

Table 7. Input parameters used to fit the HRS galaxies.

Parameter	value	Units
Pop.Synth.Mod.	Bruzual & Charlot (2003)	
Dust model	Draine & Li (2007)	
IMF	Salpeter	
Metallicity	0.02	
Velocity	40-360 in step of 10	km s ⁻¹
QF	-0.4, -0.2, 0.2, 0.4, 0.6, 0.7, 0.8, 0.9, 0.95, 1	
QA	0, 5, 10, 20, 50, 100, 150, 200, 250, 300, 400, 500, 600, 700, 800, 900, 1000, 1250, 1500, 2000, 3000	Myr
$E(B - V)_{young}$	0.05, 0.1, 0.2, 0.4	
$E(B - V)_{old}$	0.44	
Q_{PAH}	0.47, 2.50, 4.58, 6.63, 7.32	
U_{min}	0.1, 0.5, 2.0, 4.0, 8.0, 20	
α	2.0, 2.5, 3.0	
γ	0.01, 0.03, 0.1	

Note: The input parameters used in the analysis of the HRS span a wider range than those used to create the mock galaxies to avoid border effects.

bands. The systematic difference observed in the H γ pseudo filter might result from a possible contamination of the Fe and G bands in the stellar continuum (see Fig. 3). The large scatter in the Lyman continuum pseudo filter is probably due to the fact that this is the only photometric band sensitive to very young ($\lesssim 10^7$ yr) stellar populations. It is thus the most critical (and unique) band for constraining recent variations in the star formation activity of the galaxies. Indeed, the correlation between the two variables is excellent whenever $QF \leq 0.5$ (mainly unperturbed objects), while there is a systematic difference for the most perturbed galaxies ($QF > 0.8$). The systematic variation of the correlation with QF seen in Fig. 13 might be an artefact

due to the very simplistic parametrisation of the star formation law used to describe the quenching phenomenon (eq. 4). Another possible origin of the observed scatter in the Lyman continuum pseudo filter can be the fact that this observable is derived from H α + [NII] imaging data once corrected for [NII] contamination using integrated spectroscopy and for dust attenuation using the Balmer decrement whenever possible, or the 22 μ m emission from WISE otherwise (Boselli et al. 2015). All these corrections are quite uncertain.

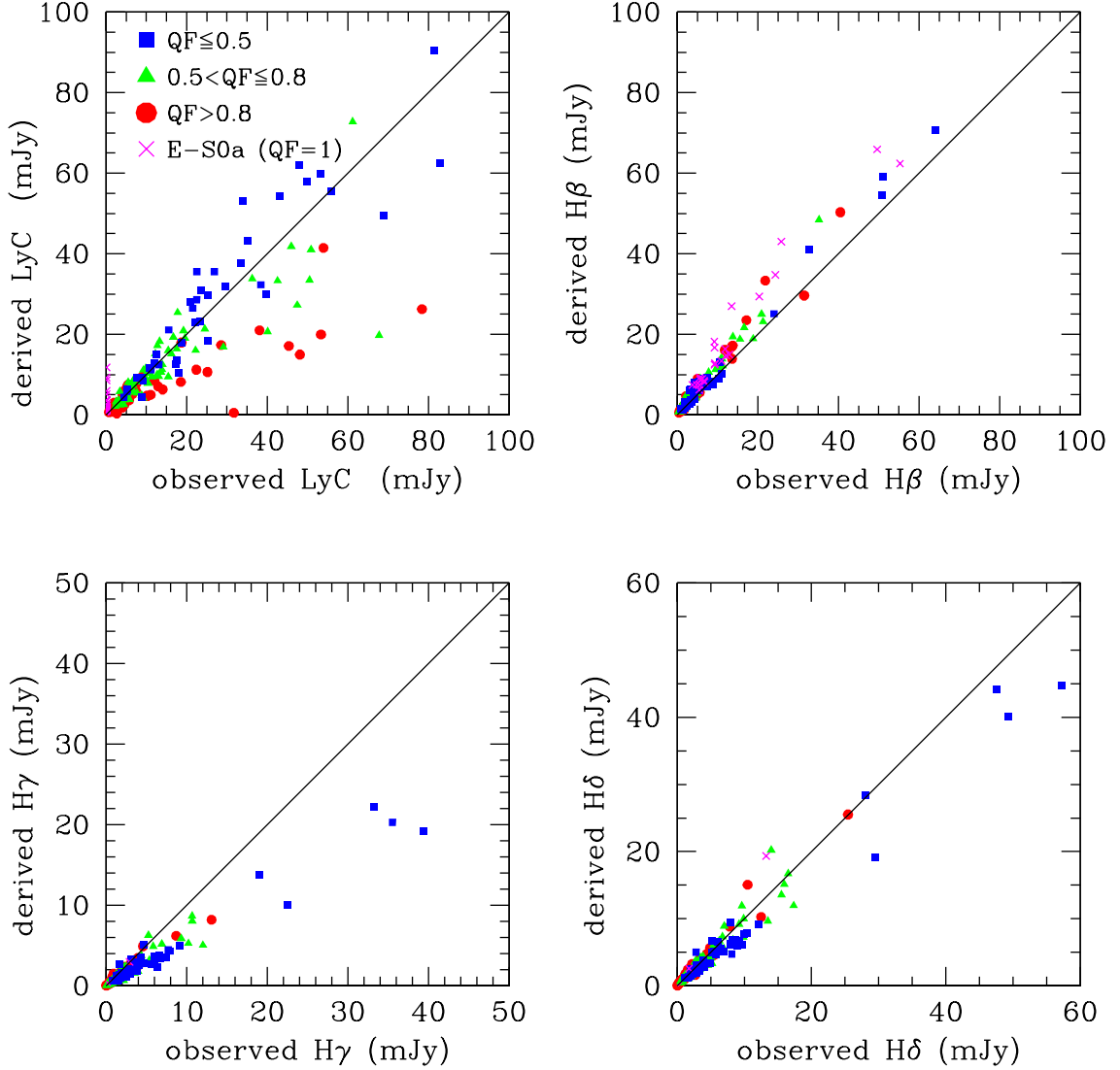


Fig. 13. Relationship between the flux densities measured within the four different pseudo filters defined in this work on the best fitted model and those measured on the observed spectra. The solid line indicates the 1:1 relation. Blue filled squares, green triangles, red circles and magenta crosses are for galaxies where the derived quenching factor is $QF \leq 0.5$, $0.5 < QF \leq 0.8$, $QF > 0.8$, and early-type galaxies (all with $QF=1$), respectively.

7. Analysis

To limit the uncertainty in the determination of the quenching age and quenching factor parameters, the analysis presented in this and in the following sections is restricted to the late-type galaxies of the HRS with available spectroscopic, *FUV*, *NUV*, and *H α* imaging data, the last opportunely corrected for dust attenuation as described in the previous sections. We recall that for all these galaxies photometric data are also available in the *gri* from SDSS, *JHK* from 2MASS, 11 and 22 μm from WISE, 100 and 160 μm from PACS and 250, 350, 500 μm from SPIRE, while *Spitzer* data at 8, 24, and 70 μm for a large fraction of the sample (see Table 2). We also analyse 22/61 of the early-type galaxies of the HRS with the same set of spectro-photometric data, with the exception of *H α* imaging data, but for which an upper limit to the *H α* emission has been derived from the spectra. As stated in sect. 2, this sample includes galaxies in different density regions, from the core of the Virgo cluster to small

groups, binary systems and relatively isolated objects in the field (Boselli et al. 2010a).

We first test whether the use of a truncated star formation history increases the quality of the SED fitting procedure of the perturbed Virgo cluster galaxies as in the case of NGC 4569 (see Fig. 10). To do that, we plot the relationship between $\chi_r^2(T)/\chi_r^2(NT)$, where $\chi_r^2(T)$ is the reduced chi-square derived using a truncated star formation history (eq. 4) and $\chi_r^2(NT)$ the one derived using an unperturbed star formation history (eq. 1), and the HI-deficiency parameter (Fig. 14), here taken as proxy for the perturbation. We recall that the typical HI-deficiency of isolated galaxies is $HI - def \lesssim 0.4$, while it increases to $HI - def \approx 1$ in the core of the Virgo cluster.

Obviously, the use of a complex star formation history characterised by two more free parameters (QF and QA) rather than a simple secular evolution increases the quality of the fit in all galaxies ($\chi_r^2(T)/\chi_r^2(NT) \leq 1$). Figure 14 shows, however, that the quality of the fit increases significantly in the most HI-deficient galaxies of the sample ($HI - def \gtrsim 0.5$) and in those objects

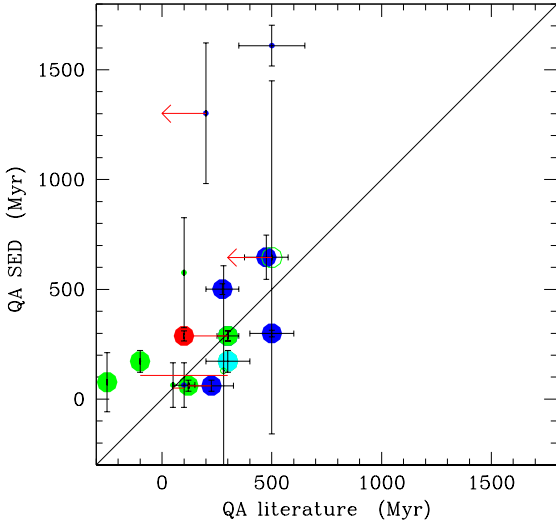


Fig. 12. Relationship between the quenching age derived using our SED fitting technique and that derived using multizone chemo-spectrophotometric models of galaxy evolution for NGC 4569 (red dot), dynamical models based on the HI and CO gas kinematics (green dots), IFU spectroscopy of the outer disc of some cluster galaxies (blue dots), and photometric data compared to population synthesis models (cyan dots). Filled symbols are used for galaxies with a quenching factor $QF > 0.5$, empty dots for those with $QF \leq 0.5$. Large symbols are for galaxies with a reduced $\chi_r^2 \leq 3$, small symbols for $\chi_r^2 > 3$. The red lines connecting two points are used to indicate those galaxies with two independent quenching ages available in the literature. The red arrows indicate upper limits to the quenching age given in the literature. The data used for this plot are given in Table 6. The solid diagonal line indicates the 1:1 relationship.

where the quenching factor is important ($QF > 0.8$). We also tested whether QF and QA , the two free parameters that we want to analyse in this work, are correlated one another, thus witnessing a possible strong degeneracy in these outputs of the model. We do not see any clear trend between these two variables.

7.1. The quenching factor

Figure 15 shows the relationship between the quenching factor QF (lower panel) and the HI-deficiency parameter. The quenching factor increases with the HI-deficiency parameter, indicating that the activity of star formation of the sample galaxies is significantly reduced once the HI gas content is removed during the interaction with the hostile cluster environment (Ciesla et al. 2016; the Spearman correlation coefficient derived for the 95 galaxies with $QF > 0.5$ and $\chi_r^2 \leq 3$ is $\rho = 0.58$). The median quenching factor of HI-deficient galaxies ($HI - def > 0.4$) is $\langle QF_{HI-def > 0.4} \rangle = 0.80 \pm 0.11$ for $\langle HI - def \rangle = 0.68 \pm 0.20$, roughly indicating that the activity of star formation of a perturbed galaxy is reduced by $\sim 80\%$ when the gas content drops by a factor of ~ 5 . For comparison, all the early-type galaxies of the sample with available spectroscopic and UV data have a quenching factor $QF = 1$. As discussed in Appendix A, these results are robust vs. the adoption of different star formation histories.

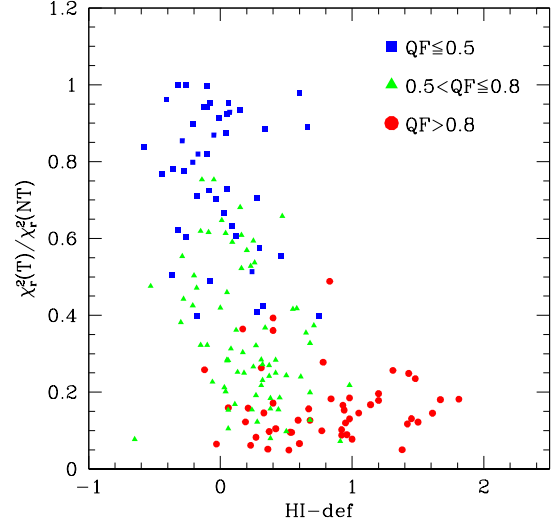


Fig. 14. Relationship between the reduced χ_r^2 ratio derived using a truncated ($\chi_r^2(T)$) to a non truncated ($\chi_r^2(NT)$) star formation history and the HI-deficiency parameter. Blue filled squares, green triangles, and red circles are for late-type galaxies with a quenching factor $QF \leq 0.5$, $0.5 < QF \leq 0.8$, and $QF > 0.8$, respectively.

7.2. The quenching age

Figure 15 also shows the relationship between the quenching age QA and the HI-deficiency parameter ($\rho = 0.48$). There is a clear relationship between the two variables, in particular if only those galaxies where QA is securely determined ($QF > 0.5$) are considered. The activity of star formation has been reduced ~ 1 Gyr ago in the most HI-deficient objects of the sample ($HI - def \gtrsim 0.8$).

Figure 16 shows the distribution of the quenching age parameter QA . The median quenching age of late-type galaxies is $QA = 135$ Myr for $0.5 < QF \leq 0.8$ and $QA = 250$ Myr for $QF > 0.8$, while that of early-type galaxies is $QA = 1320$ Myr (see Table A.1). As discussed in Appendix A, these numbers do not change significantly if the SED fitting is done leaving the rotational velocity as a free parameter. They increase by a factor of ~ 2 in the case that the quenching mechanism is parametrised with a smoothly declining star formation history.

8. Discussion

8.1. Comparison with previous studies

As discussed in sect. 5.2, the quenching ages determined in this work are comparable to those derived using independent techniques on dozen of well studied galaxies in the Virgo cluster. These timescales are also consistent with a rapid transformation of gas rich systems into quiescent objects derived from the analysis of the $NUV - i$ colour magnitude relation in the Virgo cluster and its surrounding regions (Boselli et al. 2014c; see also Cortese & Hughes 2009, Hughes & Cortese 2009) and with the most recent estimates of the galaxy infall rate in the cluster ($\sim 300 \text{ Gyr}^{-1}$ for galaxies with $M_{star} \gtrsim 10^8 M_\odot$, Boselli et al. 2008; Gavazzi et al. 2013a). These short timescales are also consistent with the presence of a long tail of extraplanar ionised gas asso-

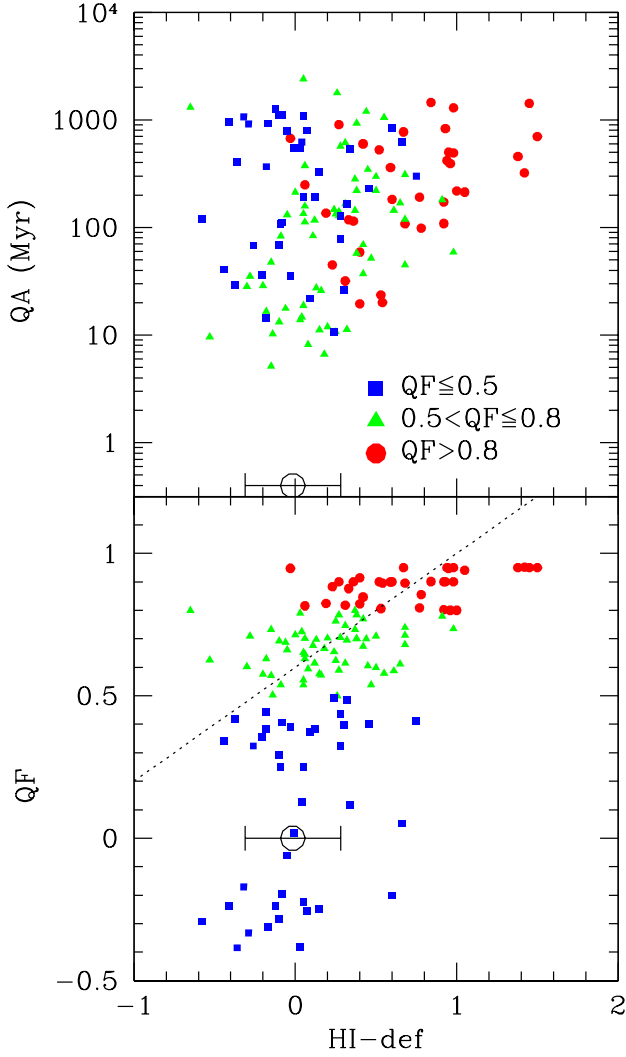


Fig. 15. Relationship between the quenching age QA (upper panel) and the quenching factor QF (lower panel) and the HI-deficiency parameter for those objects with $\chi_r^2 \leq 3$. Blue filled squares, green triangles, and red circles are for galaxies where the derived quenching factor is $QF \leq 0.5$, $0.5 < QF \leq 0.8$, and $QF > 0.8$, respectively. The large black empty symbol shows the mean value and the distribution in HI-deficiency for galaxies with a $QF \leq 0.5$ (for which the quenching factor and quenching age are arbitrarily set to $QF=0$ and $QA = 0.4$ Myr). The dotted line in the lower panel indicates the best fit found by Ciesla et al. (2016).

ciated to NGC 4569 (Boselli et al. 2016), one of the most HI-deficient Virgo cluster galaxies ($HI - def = 1.05$; Boselli et al. 2014a) characterised by a quenched star formation activity ($QF = 0.90$). The tail of ionised gas witnesses a stripping process still ongoing.

Direct observational evidences of a rapid quenching of the star formation activity of cluster galaxies are the presence of poststarburst objects in the periphery of nearby clusters such as Coma and A1367 (Poggianti et al. 2001a,b, 2004; Smith et al. 2008, 2009, 2012; Gavazzi et al. 2010). These objects are frequent also in other nearby (Fritz et al. 2014; Vulcani et al. 2015) and intermediate to high redshift clusters (Dressler et al. 1999, 2013; Balogh et al. 1999, 2011; Poggianti et al. 2004, 2009; Tran et al. 2007; Muzzin et al. 2012, 2014; Mok et al. 2013; Wu et

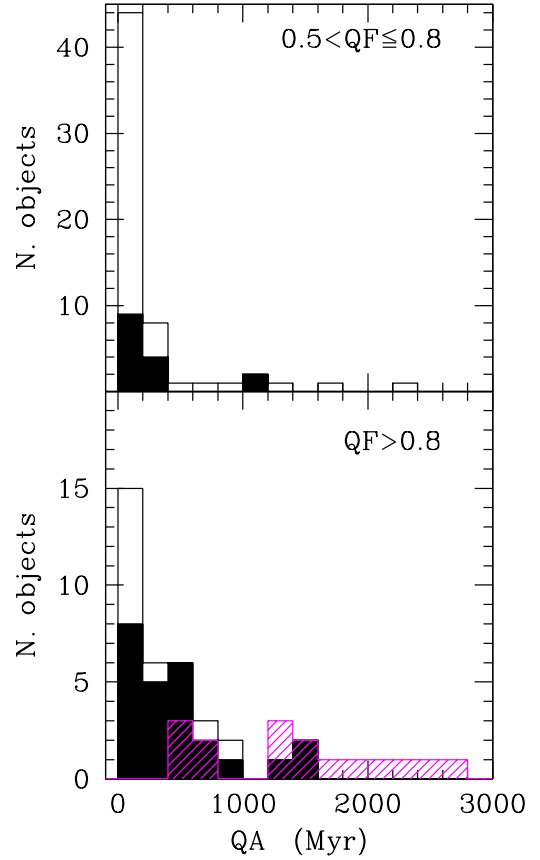


Fig. 16. Distribution of the quenching age parameter QA for galaxies with $\chi_r^2 \leq 3$ and a quenching factor $0.5 < QF \leq 0.8$ (upper panel) and $QF > 0.8$ (lower panel). The magenta histogram is for early-type galaxies, the empty histogram for all late-type galaxies, and the black shaded histogram for HI-deficient ($HI - def > 0.4$) late-type systems.

al. 2014). The frequency of these objects with a recently truncated star formation activity increases with decreasing stellar mass (Boselli & Gavazzi 2014). Evidence for a rapid transformation at intermediate redshift comes also from the analysis of the $H\alpha$ luminosity function (e.g. Kodama et al. 2004).

The analysis of large samples of nearby galaxies in different environments, from groups to massive clusters, extracted from complete surveys such as the SDSS, GALEX, or GAMA, combined with the predictions of cosmological simulations or semi-analytical models of galaxy evolution, indicate that the activity of star formation gradually and moderately decreases once galaxies become satellites of more massive galaxies on relatively long timescales (2-7 Gyr) (McGee et al. 2009; von der Linden et al. 2010; De Lucia et al. 2012). Similar results have been obtained also through the analysis of limited samples of nearby galaxies with available multifrequency data (Wolf et al. 2009; Haines et al. 2015; Paccagnella et al. 2016). More recent works suggest that after this mild decrease, the activity rapidly drops on short timescales (0.2-0.8 Gyr) once the atomic and molecular gas

content is consumed via star formation (Wetzel et al. 2012, 2013; Wijesinghe et al. 2012; Muzzin et al. 2012). Pre-processing in infalling groups is thus probably important in shaping the evolution of galaxies now members of massive clusters (Dressler 2004). The only indication for a very inefficient quenching of the star formation activity (> 9.5 Gyr) of dwarf galaxies ($10^{8.5} < M_{star} < 10^{9.5} M_{\odot}$) in relatively dense environments comes from the analysis of SDSS data combined with cosmological simulations done by Wheeler et al. (2014).

8.2. Identification of the perturbing mechanism

The typical timescales derived in the previous section and in Appendix A can be compared to those predicted by models and simulations for the identification of the dominant stripping mechanism in the nearby Virgo cluster. We recall that, given the analytical form of the star formation history used in this work (eq. 4), the quenching ages derived in the previous sections are not the typical timescales necessary to reduce the activity of star formation by a factor QF , but just the lookback time to the quenching epoch. However, since they are typically $QA \lesssim 1.3$ Gyr for $QF \leq 1$, they indicate that the timescale for quenching the activity of star formation is relatively short. This is also the case when a smoothly declining quenching process is assumed (see Appendix A).

The typical timescale for galaxy-galaxy interactions is longer than the age of the universe in dense environments such as the Virgo cluster given the large velocity dispersion of this massive system (Boselli & Gavazzi 2006). Galaxy harassment is more efficient than galaxy-galaxy interactions given the contribution of the potential well of the cluster. The simulations of Mastropietro et al. (2005), tuned to reproduce a Virgo cluster like environment for galaxies of a few $10^9 M_{\odot}$, indicate that the typical timescale necessary to heat a disc galaxy and form a pressure supported system is of a few Gyr. Unfortunately these simulations do not make any prediction on the evolution of the star formation activity, but we can expect that these timescales are comparable to those required to heat the perturbed galaxy. Again, these timescales are longer than those derived in the previous section just because the typical relaxation time in clusters such as Virgo is comparable to the age of the Universe.

In a starvation scenario, a galaxy entering a dense environment loses its halo of hot gas stopping the infall of fresh material. The activity of star formation gradually decreases after the consumption of the cold atomic and molecular gas located on the disc (Larson et al. 1980). The typical timescale for gas consumption of the HRS galaxies is ≈ 4 Gyr (Boselli et al. 2014d), and drops to $\gtrsim 3.0$ - 3.3 Gyr in gas deficient objects (Boselli et al. 2014b). These timescales, however, should be considered as lower limits since the star formation activity of the perturbed galaxies gradually decreases once the gas is removed, thus extending the time during which galaxies can still form stars. Tuned models of galaxy starvations of the representative HRS galaxy NGC 4569 (Boselli et al. 2006) or of objects with a wide range of stellar masses (Boselli et al. 2014c) consistently indicate that the starvation process requires very long timescales ($\gtrsim 6$ Gyr) to significantly reduce the star formation activity of the perturbed galaxies. Long timescales for starvations to be efficient are also indicated by numerical simulations (e.g. Bekki et al. 2002; McGee et al. 2014). This is depicted in Fig. 17, where the main sequence diagram derived using the output parameters of the SED fitting is compared to the predictions of the evolutionary models of Boselli et al. (2006, 2008, 2014c) for starvation and ram pressure stripping. Figure 17 clearly shows that, even if

the process started ~ 10 Gyr ago, starvation would never be able to reduce the star formation activity of the perturbed galaxies by $QF \gtrsim 0.5$.

Much shorter timescales for an efficient quenching of the star formation activity are instead predicted by hydrodynamic simulations (Roediger & Henseler 2005; Roediger & Bruggen 2006, 2007; Tonnesen et al. 2007; Tonnesen & Bryan 2009; Bekki 2009) and chemo-spectrophotometric models (Boselli et al. 2006; 2008; 2014c; Cortese et al. 2011) of ram pressure stripping in clusters of mass comparable to Virgo. The predictions of these chemo-spectrophotometric models derived for two different ram pressure stripping efficiencies, $\epsilon_0 = 1.2 M_{\odot} \text{ kpc}^{-2} \text{ yr}^{-1}$ necessary to reproduce the observed truncated profiles of the Virgo cluster galaxy NGC 4569 (Boselli et al. 2006), and $\epsilon_0 = 0.4 M_{\odot} \text{ kpc}^{-2} \text{ yr}^{-1}$, the mean stripping efficiency for galaxies with the typical velocity dispersion within the Virgo cluster (Boselli et al. 2008), are compared to the data in Fig. 17. The observed decrease in the star formation activity of HI-deficient galaxies (Boselli et al. 2015) in the main sequence relation can be explained by ram pressure stripping, a result similar to the one derived from the analysis of the UV-to-optical colour magnitude relation (Cortese & Hughes 2009; Hughes & Cortese 2009; Boselli et al. 2014c,d). The large number of objects below the main sequence drawn by unperturbed systems, often taken as an indication that the perturbing process lasts several Gyrs, is due to the large infall rate of star forming systems observed in Virgo ($\approx 300 \text{ Gyr}^{-1}$; Tully & Shaya 1984; Boselli et al. 2008; Gavazzi et al. 2013a). A further evidence in agreement with the ram pressure stripping scenario is given in Fig. 18, where the fraction of late-type galaxies with a quenching factor $QF > 0.8$ and an HI-deficiency $HI - def > 0.4$ are plotted versus the distance from the core of the Virgo cluster. Figure 18 clearly shows that both fractions drop by a factor of ≈ 5 from the core of the cluster ($R/R_{vir} < 0.5$), where the hot X-ray gas is detected by *ROSAT* (Bohringer et al. 1994), to the cluster periphery ($R/R_{vir} \gtrsim 4$), in agreement with models and simulations (Tonnesen et al. 2007; Bahe et al. 2013; Cen et al. 2014). The recent observations of nearby clusters with 4-8 m class telescopes equipped with wide field panoramic detectors and narrow band filters is revealing the presence up to the cluster virial radius of several star forming galaxies with long tails of ionised gas typically produced by a ram pressure stripping event (Gavazzi et al. 2001; Sun et al. 2007; Yagi et al. 2010; Fossati et al. 2012). Two galaxies with long tails of HI gas have been also observed in the periphery of A1367, outside the virial radius (Scott et al. 2012). The radial variation of the fraction of quenched and HI-deficient galaxies is consistent with the one observed in the Virgo cluster out to large distances by Gavazzi et al. (2013a) and Boselli et al. (2014c), a further evidence that quenching is a rapid process (Boselli et al. 2014c).

Short timescales are also consistent with a recent formation of the faint end of the red sequence (De Lucia et al. 2007, 2009; Stott et al. 2007, 2009; Gilbank & Balogh 2008).

8.3. Rapid or slow environmental quenching?

We often read in the literature that the environmental quenching acts on long timescales (McGee et al. 2009; von der Linden et al. 2010; De Lucia et al. 2012; Taranu et al. 2014; Haines et al. 2015; Paccagnella et al. 2016). This apparent disagreement with our results comes from the fact that different definitions of quenching timescales are often used. In those studies based on the combined analysis of statistical samples extracted from all sky surveys such as the SDSS with the predictions of cos-

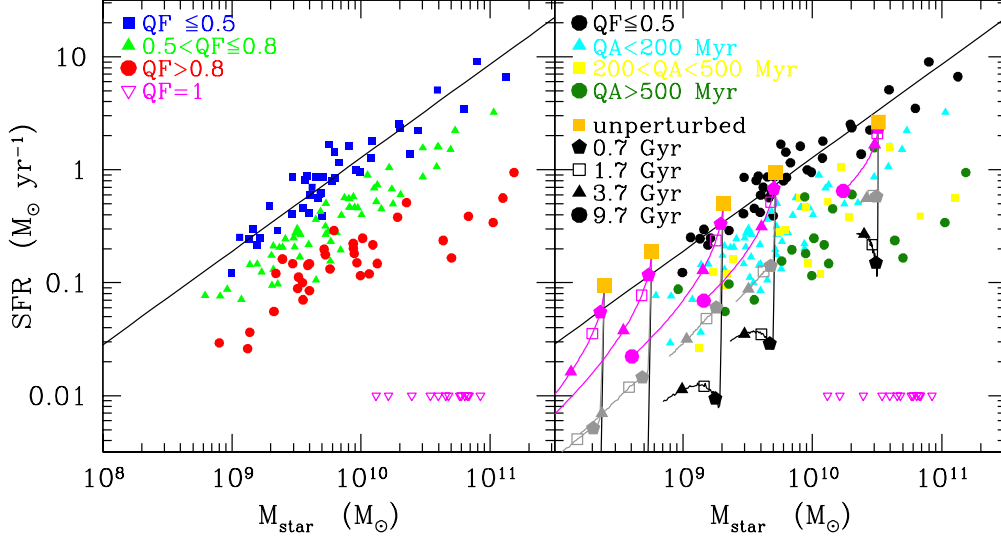


Fig. 17. Relationship between the present day star formation rate and the stellar mass (main sequence) derived from the SED fitting code. Left panel: symbols are coded according to the quenching factor of the analysed galaxies. Blue filled squares, green triangles, and red circles are for galaxies where the derived quenching factor is $QF \leq 0.5$, $0.5 < QF \leq 0.8$, and $QF > 0.8$, respectively. Magenta triangles indicate upper limits to the star formation rate of early-type galaxies. The solid line shows the bisector fit to the data for unperturbed galaxies ($QF \leq 0.5$). Right panel: same relation with colour symbols coded according to the quenching age. Black filled dots are for unperturbed galaxies ($QF \leq 0.5$), cyan triangles, yellow squares, and dark green dots for galaxies with a quenching age $QA < 200$ Myr, $200 < QA < 500$ Myr, and $QA > 500$ Myr, respectively. The large orange filled squares indicate the models of Boselli et al. (2006, 2014c) for unperturbed galaxies of spin parameter $\lambda=0.05$ and rotational velocity 70, 100, 130, 170, and 220 km s^{-1} . The magenta lines indicate the starvation models. The black and grey lines show the ram pressure stripping models for a stripping efficiency $\epsilon_0 = 1.2 M_{\odot} \text{ kpc}^{-2} \text{ yr}^{-1}$ and $\epsilon_0 = 0.4 M_{\odot} \text{ kpc}^{-2} \text{ yr}^{-1}$, respectively. Different symbols along the models indicate the position of the model galaxies at a given look-back time from the beginning of the interaction.

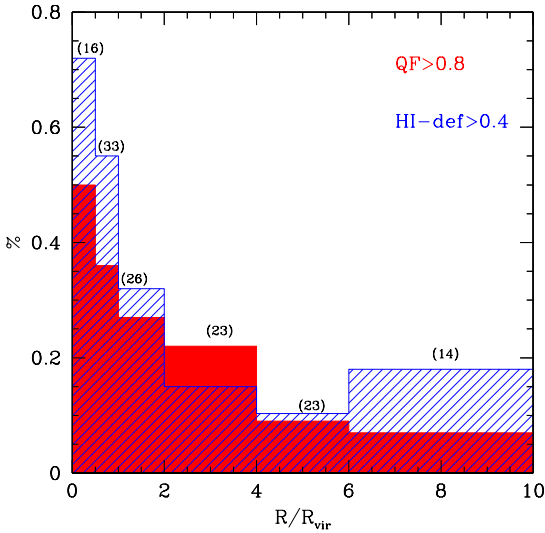


Fig. 18. Variation of the fraction of late-type galaxies with a quenching factor $QF > 0.8$ (red histogram) and an HI-deficiency $HI-def > 0.4$ (blue shaded histogram) and the distance from the centre of the Virgo cluster, in units of virial radii. The number galaxies for each bin of distance is given in parenthesis.

mological simulations or semi analytical models, the quenching timescale is often defined as the time necessary to stop the activity of star formation of a galaxy once it becomes satellite of a larger system. Since the recent accretion of late-type galaxies in nearby clusters occurs principally through smaller groups (Gnedin 2003; McGee et al. 2009; De Lucia et al. 2010), this timescale is necessary long even if the quenching of the activity happens on short timescales only once the galaxy fall in the main cluster structure. Indeed, the analysis of Wetzel et al. (2013) suggests a different evolution of the star formation activity of galaxies, first mildly declining on long timescales (2-4 Gyr), then with a rapid decrease (0.2-0.8 Gyr) ('delayed-then-rapid'). The timescales that we estimate in this work, as those derived for other Virgo cluster galaxies as described in sect. 5.2, are rather representative of the timescale since the first stripping of the cold gas on the disc, which generally occurs once the galaxy is close to the pericenter along its orbit within the cluster. Recently, Oman & Hudson (2016) studied the quenching timescale and efficiency in massive clusters ($M_{\text{cluster}} > 10^{13} M_{\odot}$) by comparing N-body simulations with the observed properties of SDSS galaxies. This work indicates that the quenching is 100% efficient ($QF = 1$) and occurs in the core of the cluster, at or near the first pericenter approach. These results convincingly point at ram pressure stripping as the main quenching mechanism in massive haloes. While their quenching timescale is the typical value for a population of galaxies in clusters, their

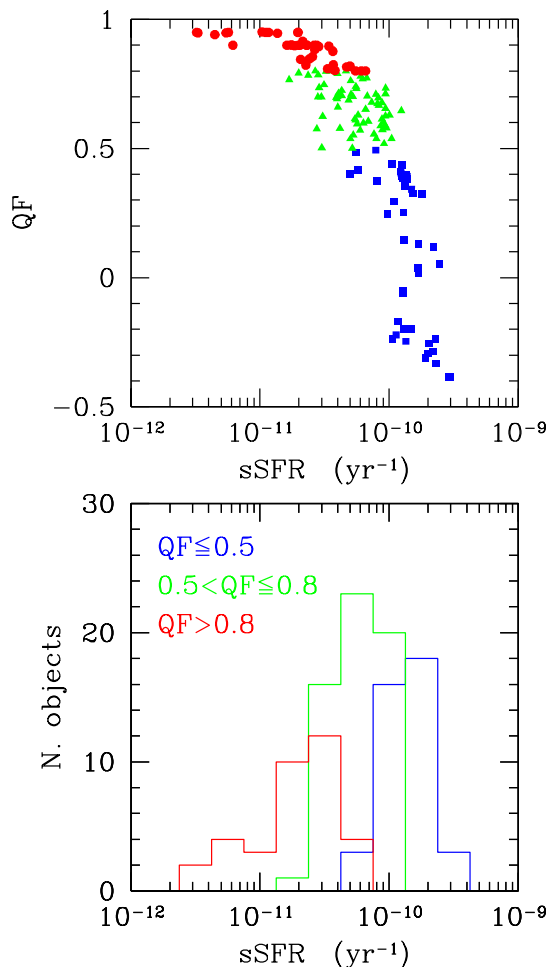


Fig. 19. Upper panel: relationship between the quenching factor QF and the specific star formation activity $sSFR$ for the late type galaxies of the sample with a reduced $\chi_r^2 \leq 3$. Blue filled squares, green triangles, and red circles are for galaxies where the derived quenching factor is $QF \leq 0.5$, $0.5 < QF \leq 0.8$, and $QF > 0.8$, respectively. Lower panel: $sSFR$ distribution for different quenching factors.

results are in excellent agreement with our study of the histories of individual galaxies in Virgo.

It is also worth remembering that the dominant perturbing mechanism is expected to change as a function of the mass of the infalling galaxy and on quantities that strongly depend on the total dynamical mass of the cluster such as the velocity dispersion of galaxies within the cluster, and the density and temperature of the intracluster gas. These quantities might also vary locally within the cluster since the distribution of the intracluster medium is not uniform in terms of density and turbulence. Since all these parameters change also with redshift, we expect to have different results for different environments at different epochs, as indeed observed (e.g. Balogh et al. 2016).

A further possible origin of the apparent disagreement between the short timescales derived in this work with those given in the literature might be due to the definition of quenched galaxies. Here we consider quenched galaxies those objects with an activity of star formation reduced by a factor of $QF > 0.5$ or

$QF > 0.8$. These are still star forming late-type galaxies. As depicted in Fig. 19, their typical specific star formation rate, defined as the current star formation rate divided by the total stellar mass given by the fit, ranges from a few 10^{-12} yr^{-1} to $sSFR \lesssim 10^{-10} \text{ yr}^{-1}$. A typical example is the massive NGC 4569 in the core of the Virgo cluster ($sSFR = 4.5 \times 10^{-11} \text{ yr}^{-1}$), characterised by a prominent $H\alpha$ emission witnessing an ongoing star formation activity. In SDSS based works such as Wetzel et al. (2012, 2013), quenched galaxies are those with a specific star formation rate $sSFR \lesssim 10^{-11} \text{ yr}^{-1}$, a much more stringent definition than the one used in this work. This difference is important in the framework of galaxy evolution. In a ram pressure stripping scenario, models and simulations indicate that most of the gas is stripped from the disc of spiral galaxies on short timescales ($\lesssim 0.2$ Gyr) when the galaxy is at the pericenter along its orbit (Roediger & Henseler 2005; Roediger & Bruggen 2006, 2007; Tonnesen et al. 2007; Tonnesen & Bryan 2009). At this stage, however, there is still gas to sustain a moderate star formation activity on the inner disc of the perturbed galaxies (Boselli et al. 2006; Tonnesen & Bryan 2012; Bekki 2014; Roediger et al. 2015). Their quenching factor is thus $QF < 1$ and their specific star formation activity $sSFR \gtrsim 10^{-11} \text{ yr}^{-1}$. The complete stripping of the gas, thus the total quenching of the star formation activity ($QF = 1$), requires longer timescales (1-3 Gyr), consistent with what found for the 22 early-type galaxies of the HRS. These timescales are fairly comparable to the timescale for the rapid quenching of the star formation activity of galaxies in rich environments found by Wetzel et al. (2012, 2013) and Oman & Hudson (2016) in the local universe and by Muzzin et al. (2014) and Mok et al. (2014) at $z \sim 1$.

It seems thus that the origin of most of the tension between these works is in the definition of the quenching time, here defined as the epoch when galaxies drastically reduced ($\gtrsim 50\%$) their activity of star formation, in Wetzel et al. (2012, 2013) and in other works the time since a galaxy *first* became a satellite of a massive halo.

We conclude by mentioning that this analysis indicates that the quenching time can be accurately derived using our SED fitting technique only in 30% of the sample (those galaxies with $QF > 0.8$), a value comparable to the number of HI-deficient objects ($HI-def > 0.4$; 33%) or of late-type galaxies located within one virial radius of Virgo (36%). Whenever the perturbing mechanism is milder than in Virgo, as it is probably the case in less massive haloes, we expect a less efficient quenching episode ($QF \ll 1$). For these galaxies it is hard to break all the degeneracies between star formation history, IMF, metallicity, and dust attenuation, and thus derive accurate quenching timescales even using a UV-to-FIR SED fitting code as done in this work.

9. Conclusion

We study the star formation history of the *Herschel* Reference Survey, a K -band-selected, volume-limited complete sample of nearby galaxies using the CIGALE SED fitting code. The sample includes objects in the Virgo cluster and is thus perfectly suited for understanding the role of the environment on galaxy evolution. To quantify the perturbation induced by the interaction with the hostile environment on the star formation activity of cluster galaxies, we adopt a truncated star formation history where the secular evolution is parametrised using the chemospectrophotometric physically justified models of Boissier & Prantzos (2000). To constrain any possible abrupt variation of the star formation activity of the Virgo cluster galaxies, we combine the UV to far infrared photometric data (20 bands) with age

sensitive Balmer absorption line indices extracted from medium resolution ($R \sim 1000$) integrated spectroscopy (3 bands) and $H\alpha$ imaging data (1 band). $H\alpha$ fluxes are compulsory to constraint variations occurred at very recent epochs ($\lesssim 100$ Myr). The best fit to the data gives the quenching factor QF and the quenching age QA . The first parameter quantifies how much the star formation activity has been reduced during the interaction ($QF=0$ for unperturbed systems, $QF = 1$ when the star formation activity has been completely stopped), while QA gives the lookback time of the epoch of the quenching episode. We checked the reliability of the output parameters using mock catalogues of simulated galaxies and different star formation histories.

The analysis of the sample brought to the following results:

1) The quality of the SED fitting significantly increases using a truncated star formation history in all the HI-deficient galaxies of the sample, where the interaction with the hostile environment removed a large fraction of the cold gas necessary to feed star formation.

2) In these HI-deficient objects the activity of star formation is reduced by a factor of $50\% \leq QF < 80\%$ on timescales of ≈ 135 Myr, and $QF \geq 80\%$ on timescales of ≈ 250 Myr, while it is fully stopped after ≈ 1.3 Gyr in early-type galaxies. These timescales are a factor of ≈ 2 longer if a smoothly declining quenching process is assumed.

3) The fraction of quenched late-type galaxies ($QF \geq 80\%$), as the fraction of HI-deficient objects, decreases by a factor of ≈ 5 from the core of the Virgo cluster ($R/R_{vir} \leq 0.5$) to the cluster periphery ($R/R_{vir} \geq 4$).

The disagreement with the results obtained from the analysis of large samples such as the SDSS (e.g. Wetzel et al. 2012, 2013), which indicate longer timescales with a delayed-then-rapid quenching process, is only apparent since our timescales are representative of the rapid decrease of the star formation activity occurred when galaxies enter the rich Virgo cluster, while those given in the literature of the time since a galaxy became a satellite of a more massive halo. Furthermore, our are the timescales necessary to reduce the star formation activity by a factor of $\geq 50\text{-}80\%$, while those given in the literature to fully stop the activity of the perturbed galaxies. All these results are consistent with a rapid quenching of the star formation activity of the late-type galaxies recently accreted on the Virgo cluster as predicted by ram pressure stripping models. These results discard inefficient mechanisms such as starvation, which require very long (≥ 6 Gyr) timescales to significantly quench the star formation activity of the perturbed galaxies.

Acknowledgements. We thank the anonymous referee for constructive comments which improved the clarity of the manuscript. This research has been financed by the French national program PNCG. M. Fossati acknowledges the support of the Deutsche Forschungsgemeinschaft via Project ID 3871/1-1. L. Ciesla acknowledges funding from the European Union Seventh Framework Programme (FP7/2007-2013) under grant agreement n 312725. This research has made use of the NASA/IPAC Extragalactic Database (NED) which is operated by the Jet Propulsion Laboratory, California Institute of Technology, under contract with the National Aeronautics and Space Administration.

References

- Abramson, A., & Kenney, J. D. P. 2014, *AJ*, 147, 63
 Abramson, A., Kenney, J. D. P., Crowl, H. H., et al. 2011, *AJ*, 141, 164
 Baes, M., Clemens, M., Xilouris, E. M., et al. 2010, *A&A*, 518, L53
 Bahé, Y. M., McCarthy, I. G., Balogh, M. L., & Font, A. S. 2013, *MNRAS*, 430, 3017
 Balogh, M. L., Morris, S. L., Yee, H. K. C., Carlberg, R. G., & Ellingson, E. 1999, *ApJ*, 527, 54
 Balogh, M. L., McGee, S. L., Mok, A., et al. 2016, *MNRAS*, 456, 4364
 Bekki, K. 2009, *MNRAS*, 399, 2221
 Bekki, K. 2014, *MNRAS*, 438, 444
 Bekki, K., Couch, W. J., & Shioya, Y. 2002, *ApJ*, 577, 651
 Bendo, G. J., Galliano, F., & Madden, S. C. 2012, *MNRAS*, 423, 197
 Bigiel, F., Leroy, A., Walter, F., et al. 2008, *AJ*, 136, 2846
 Böhringer, H., Briel, U. G., Schwarz, R. A., et al. 1994, *Nature*, 368, 828
 Boissier, S., & Prantzos, N. 1999, *MNRAS*, 307, 857
 Boissier, S., & Prantzos, N. 2000, *MNRAS*, 312, 398
 Boissier, S., & Prantzos, N. 2001, *MNRAS*, 325, 321
 Boissier, S., Boselli, A., Prantzos, N., & Gavazzi, G. 2001, *MNRAS*, 321, 733
 Boissier, S., Prantzos, N., Boselli, A., & Gavazzi, G. 2003, *MNRAS*, 346, 1215
 Boquien, M., Buat, V., Boselli, A., et al. 2012, *A&A*, 539, A145
 Boquien, M., Boselli, A., Buat, V., et al. 2013, *A&A*, 554, A14
 Boquien, M., Buat, V., & Perret, V. 2014, *A&A*, 571, A72
 Boquien, M., Kennicutt, R., Calzetti, D., et al. 2016, *A&A*, 591, A6
 Boselli, A. 2011, *A Panchromatic View of Galaxies*, by Alessandro Boselli. - Practical Approach Book - ISBN-10: 3-527-40991-2. ISBN-13: 978-3-527-40991-4 - Wiley-VCH, Berlin 2011. XVI, 324pp, Hardcover.
 Boselli, A., & Gavazzi, G. 2006, *PASP*, 118, 517
 Boselli, A., & Gavazzi, G. 2009, *A&A*, 508, 201
 Boselli, A., & Gavazzi, G. 2014, *A&A Rev.*, 22, 74
 Boselli, A., Gavazzi, G., Donas, J., & Scodreggio, M. 2001, *AJ*, 121, 753
 Boselli, A., Lequeux, J., & Gavazzi, G. 2002, *A&A*, 384, 33
 Boselli, A., Boissier, S., Cortese, L., et al. 2005b, *ApJ*, 623, L13
 Boselli, A., Boissier, S., Cortese, L., et al. 2006, *ApJ*, 651, 811
 Boselli, A., Boissier, S., Cortese, L., & Gavazzi, G. 2008, *ApJ*, 674, 742
 Boselli, A., Boissier, S., Cortese, L., et al. 2009, *ApJ*, 706, 1527
 Boselli, A., Eales, S., Cortese, L., et al. 2010a, *PASP*, 122, 261
 Boselli, A., Ciesla, L., Buat, V., et al. 2010b, *A&A*, 518, L61
 Boselli, A., Boissier, S., Heinis, S., et al. 2011, *A&A*, 528, A107
 Boselli, A., Ciesla, L., Cortese, L., et al. 2012, *A&A*, 540, A54
 Boselli, A., Hughes, T. M., Cortese, L., Gavazzi, G., & Buat, V. 2013, *A&A*, 550, A114
 Boselli, A., Cortese, L., & Boquien, M. 2014a, *A&A*, 564, A65
 Boselli, A., Cortese, L., Boquien, M., et al. 2014b, *A&A*, 564, A67
 Boselli, A., Voyer, E., Boissier, S., et al. 2014c, *A&A*, 570, AA69
 Boselli, A., Cortese, L., Boquien, M., et al. 2014d, *A&A*, 564, A66
 Boselli, A., Fossati, M., Gavazzi, G., et al. 2015, *A&A*, 579, A102
 Boselli, A., Cuillandre, J. C., Fossati, M., et al. 2016, *A&A*, 587, A68
 Brinchmann, J., Charlot, S., White, S. D. M., et al. 2004, *MNRAS*, 351, 1151
 Bruzual, G., & Charlot, S. 2003, *MNRAS*, 344, 1000
 Buat, V., Boissier, S., Burgarella, D., et al. 2008, *A&A*, 483, 107
 Buat, V., Heinis, S., Boquien, M., et al. 2014, *A&A*, 561, A39
 Byrd, G., & Valtonen, M. 1990, *ApJ*, 350, 89
 Cayatte, V., van Gorkom, J. H., Balkowski, C., & Kotanyi, C. 1990, *AJ*, 100, 604
 Cen, R., Pop, A. R., & Bahcall, N. A. 2014, *Proceedings of the National Academy of Science*, 111, 7914
 Chevillard, J., & Charlot, S. 2016, *MNRAS*, 462, 1415
 Ciesla, L., Boselli, A., Smith, M. W. L., et al. 2012, *A&A*, 543, A161
 Ciesla, L., Boquien, M., Boselli, A., et al. 2014, *A&A*, 565, A128
 Ciesla, L., Boselli, A., Elbaz, D., et al. 2016, *A&A*, 585, A43
 Colless, M., & Dunn, A. M. 1996, *ApJ*, 458, 435
 Cortés, J. R., Kenney, J. D. P., & Hardy, E. 2015, *ApJS*, 216, 9
 Cortese, L., Davies, J. I., Pohlen, M., et al. 2010, *A&A*, 518, L49
 Cortese, L., Catinella, B., Boissier, S., Boselli, A., & Heinis, S. 2011, *MNRAS*, 415, 1797
 Cortese, L., Ciesla, L., Boselli, A., et al. 2012a, *A&A*, 540, A52
 Cortese, L., Boissier, S., Boselli, A., et al. 2012b, *A&A*, 544, A101
 Cortese, L., Fritz, J., Bianchi, S., et al. 2014, *MNRAS*, 440, 942
 Cortese, L., Bekki, K., Boselli, A., et al. 2016, *MNRAS*,
 Cowie, L. L., & Songaila, A. 1977, *Nature*, 266, 501
 Crowl, H. H., & Kenney, J. D. P. 2008, *AJ*, 136, 1623
 da Cunha, E., Charlot, S., & Elbaz, D. 2008, *MNRAS*, 388, 1595
 Davis, T. A., Alatalo, K., Bureau, M., et al. 2013, *MNRAS*, 429, 534
 De Lucia, G., Poggianti, B. M., Aragón-Salamanca, A., et al. 2004, *ApJ*, 610, L77
 De Lucia, G., Poggianti, B. M., Aragón-Salamanca, A., et al. 2007, *MNRAS*, 374, 809
 De Lucia, G., Poggianti, B. M., Halliday, C., et al. 2009, *MNRAS*, 400, 68
 De Lucia, G., Weinmann, S., Poggianti, B. M., Aragón-Salamanca, A., & Zaritsky, D. 2012, *MNRAS*, 423, 1277
 den Heijer, M., Oosterloo, T. A., Serra, P., et al. 2015, *A&A*, 581, A98
 Draine, B. T., & Li, A. 2007, *ApJ*, 657, 810
 Draine, B. T., Dale, D. A., Bendo, G., et al. 2007, *ApJ*, 663, 866
 Dressler, A. 1980, *ApJ*, 236, 351
 Dressler, A. 2004, *Clusters of Galaxies: Probes of Cosmological Structure and Galaxy Evolution*, 206
 Dressler, A., Oemler, A., Jr., Couch, W. J., et al. 1997, *ApJ*, 490, 577
 Dressler, A., Smail, I., Poggianti, B. M., et al. 1999, *ApJS*, 122, 51

- Dressler, A., Oemler, A., Jr., Poggianti, B. M., et al. 2013, *ApJ*, 770, 62
- Falcón-Barroso, J., Bacon, R., Bureau, M., et al. 2006, *MNRAS*, 369, 529
- Font, A. S., Bower, R. G., McCarthy, I. G., et al. 2008, *MNRAS*, 389, 1619
- Fontanot, F., De Lucia, G., Monaco, P., Somerville, R. S., & Santini, P. 2009, *MNRAS*, 397, 1776
- Fossati, M., Gavazzi, G., Boselli, A., & Fumagalli, M. 2012, *A&A*, 544, A128
- Fossati, M., Gavazzi, G., Savorgnan, G., et al. 2013, *A&A*, 553, A91
- Fritz, J., Poggianti, B. M., Cava, A., et al. 2014, *A&A*, 566, A32
- Fumagalli, M., Krumholz, M. R., Prochaska, J. X., Gavazzi, G., & Boselli, A. 2009, *ApJ*, 697, 1811
- Gavazzi, G. 1987, *ApJ*, 320, 96
- Gavazzi, G., Catinella, B., Carrasco, L., Boselli, A., & Contursi, A. 1998, *AJ*, 115, 1745
- Gavazzi, G., Boselli, A., Mayer, L., et al. 2001, *ApJ*, 563, L23
- Gavazzi, G., Boselli, A., Pedotti, P., Gallazzi, A., & Carrasco, L. 2002a, *A&A*, 396, 449
- Gavazzi, G., Bonfanti, C., Sanvito, G., Boselli, A., & Scodreggio, M. 2002b, *ApJ*, 576, 135
- Gavazzi, G., Zaccardo, A., Sanvito, G., Boselli, A., & Bonfanti, C. 2004, *A&A*, 417, 499
- Gavazzi, G., Boselli, A., van Driel, W., & O'Neil, K. 2005, *A&A*, 429, 439
- Gavazzi, G., O'Neil, K., Boselli, A., & van Driel, W. 2006a, *A&A*, 449, 929
- Gavazzi, G., Boselli, A., Cortese, L., et al. 2006b, *A&A*, 446, 839
- Gavazzi, G., Fumagalli, M., Cucciati, O., & Boselli, A. 2010, *A&A*, 517, A73
- Gavazzi, G., Fumagalli, M., Fossati, M., et al. 2013a, *A&A*, 553, A89
- Gavazzi, G., Savorgnan, G., Fossati, M., et al. 2013b, *A&A*, 553, A90
- Gilbank, D. G., & Balogh, M. L. 2008, *MNRAS*, 385, L116
- Gnedin, O. Y. 2003, *ApJ*, 589, 752
- Gunn, J. E., & Gott, J. R., III 1972, *ApJ*, 176, 1
- Guo, Q., White, S., Boylan-Kolchin, M., et al. 2011, *MNRAS*, 413, 101
- Haines, C. P., Pereira, M. J., Smith, G. P., et al. 2015, *ApJ*, 806, 101
- Haynes, M. P., & Giovanelli, R. 1984, *AJ*, 89, 758
- Haynes, M. P., Giovanelli, R., & Chincarini, G. L. 1984, *ARA&A*, 22, 445
- Henriques, B. M. B., White, S. D. M., Thomas, P. A., et al. 2015, *MNRAS*, 451, 2663
- Hirschmann, M., De Lucia, G., Wilman, D., et al. 2014, *MNRAS*, 444, 2938
- Jarrett, T. H., Chester, T., Cutri, R., Schneider, S. E., & Huchra, J. P. 2003, *AJ*, 125, 525
- Kang, X., & van den Bosch, F. C. 2008, *ApJ*, 676, L101
- Kauffmann, G., Heckman, T. M., White, S. D. M., et al. 2003, *MNRAS*, 341, 54
- Kenney, J. D. P., van Gorkom, J. H., & Vollmer, B. 2004, *AJ*, 127, 3361
- Kenney, J. D. P., Geha, M., Jáchym, P., et al. 2014, *ApJ*, 780, 119
- Kennicutt, R. C., Jr. 1983, *AJ*, 88, 483
- Kennicutt, R. C., Jr. 1998a, *ApJ*, 498, 541
- Kennicutt, R. C., Jr. 1998b, *ARA&A*, 36, 189
- Kennicutt, R. C., Jr., Armus, L., Bendo, G., et al. 2003, *PASP*, 115, 928
- Kimm, T., Somerville, R. S., Yi, S. K., et al. 2009, *MNRAS*, 394, 1131
- Kodama, T., Balogh, M. L., Smail, I., Bower, R. G., & Nakata, F. 2004, *MNRAS*, 354, 1103
- Koopmann, R. A., & Kenney, J. D. P. 2004, *ApJ*, 613, 866
- Larson, R. B., Tinsley, B. M., & Caldwell, C. N. 1980, *ApJ*, 237, 692
- Levesque, E. M., Leitherer, C., Ekstrom, S., Meynet, G., & Schaerer, D. 2012, *ApJ*, 751, 67
- López Fernández, R., Cid Fernandes, R., González Delgado, R. M., et al. 2016, *MNRAS*, 458, 184
- Mastropietro, C., Moore, B., Mayer, L., et al. 2005, *MNRAS*, 364, 607
- McGee, S. L., Balogh, M. L., Bower, R. G., Font, A. S., & McCarthy, I. G. 2009, *MNRAS*, 400, 937
- McGee, S. L., Bower, R. G., & Balogh, M. L. 2014, *MNRAS*, 442, L105
- McLaughlin, D. E. 1999, *ApJ*, 512, L9
- Merritt, D. 1983, *ApJ*, 264, 24
- Mok, A., Balogh, M. L., McGee, S. L., et al. 2013, *MNRAS*, 431, 1090
- Moore, B., Lake, G., & Katz, N. 1998, *ApJ*, 495, 139
- Moustakas, J., Kennicutt, R. C., Jr., Tremonti, C. A., et al. 2010, *ApJS*, 190, 233-266
- Muñoz-Mateos, J. C., Gil de Paz, A., Boissier, S., et al. 2007, *ApJ*, 658, 1006
- Muñoz-Mateos, J. C., Gil de Paz, A., Boissier, S., et al. 2009, *ApJ*, 701, 1965-1991
- Muñoz-Mateos, J. C., Boissier, S., Gil de Paz, A., et al. 2011, *ApJ*, 731, 10
- Muzzin, A., Wilson, G., Yee, H. K. C., et al. 2012, *ApJ*, 746, 188
- Muzzin, A., van der Burg, R. F. J., McGee, S. L., et al. 2014, *ApJ*, 796, 65
- Newman, A. B., Ellis, R. S., Andreon, S., et al. 2014, *ApJ*, 788, 51
- Noll, S., Burgarella, D., Giovannoli, E., et al. 2009, *A&A*, 507, 1793
- Nulsen, P. E. J. 1982, *MNRAS*, 198, 1007
- Nulsen, P. E. J., & Bohringer, H. 1995, *MNRAS*, 274, 1093
- Oman, K. A., & Hudson, M. J. 2016, [arXiv:1607.07934](https://arxiv.org/abs/1607.07934)
- Osterbrock, D. E., & Ferland, G. J. 2006, *Astrophysics of gaseous nebulae and active galactic nuclei*, 2nd. ed. by D.E. Osterbrock and G.J. Ferland. Sausalito, CA: University Science Books, 2006,
- Paccagnella, A., Vulcani, B., Poggianti, B. M., et al. 2016, *ApJ*, 816, L25
- Pacifici, C., Charlot, S., Blaizot, J., & Brinchmann, J. 2012, *MNRAS*, 421, 2002
- Pacifici, C., da Cunha, E., Charlot, S., et al. 2015, *MNRAS*, 447, 786
- Poggianti, B. M., & Barbaro, G. 1997, *A&A*, 325, 1025
- Poggianti, B. M., Bridges, T. J., Carter, D., et al. 2001a, *ApJ*, 563, 118
- Poggianti, B. M., Bridges, T. J., Mobasher, B., et al. 2001b, *ApJ*, 562, 689
- Poggianti, B. M., Bridges, T. J., Komiyama, Y., et al. 2004, *ApJ*, 601, 197
- Poggianti, B. M., Aragón-Salamanca, A., Zaritsky, D., et al. 2009, *ApJ*, 693, 112
- Roediger, E., & Hensler, G. 2005, *A&A*, 433, 875
- Roediger, E., & Brügggen, M. 2006, *MNRAS*, 369, 567
- Roediger, E., & Brügggen, M. 2007, *MNRAS*, 380, 1399
- Roediger, E., Brügggen, M., Owers, M. S., Ebeling, H., & Sun, M. 2014, *MNRAS*, 443, L114
- Sandage, A. 1986, *A&A*, 161, 89
- Sarazin, C. L. 1986, *Reviews of Modern Physics*, 58, 1
- Sarzi, M., Falcón-Barroso, J., Davies, R. L., et al. 2006, *MNRAS*, 366, 1151
- Schindler, S., Binggeli, B., Böhringer, H. 1999, *A&A*, 343, 420
- Schmidt, M. 1959, *ApJ*, 129, 243
- Scott, T. C., Cortese, L., Brinks, E., et al. 2012, *MNRAS*, 419, L19
- Silva, L., Granato, G. L., Bressan, A., & Danese, L. 1998, *ApJ*, 509, 103
- Skrutskie, M. F., Cutri, R. M., Stiening, R., et al. 2006, *AJ*, 131, 1163
- Smith, R. J., Marzke, R. O., Hornschemeier, A. E., et al. 2008, *MNRAS*, 386, L96
- Smith, R. J., Lucey, J. R., Hudson, M. J., et al. 2009, *MNRAS*, 392, 1265
- Smith, R. J., Lucey, J. R., Price, J., Hudson, M. J., & Phillipps, S. 2012, *MNRAS*, 419, 3167
- Solanes, J. M., Manrique, A., García-Gómez, C., et al. 2001, *ApJ*, 548, 97
- Stott, J. P., Smail, I., Edge, A. C., et al. 2007, *ApJ*, 661, 95
- Stott, J. P., Pimblett, K. A., Edge, A. C., Smith, G. P., & Wardlow, J. L. 2009, *MNRAS*, 394, 2098
- Sun, M., Donahue, M., & Voit, G. M. 2007, *ApJ*, 671, 190
- Taranu, D. S., Hudson, M. J., Balogh, M. L., et al. 2014, *MNRAS*, 440, 1934
- Thomas, R., Le Fevre O., Scodreggio M., et al. 2016, [arXiv:1602.01841](https://arxiv.org/abs/1602.01841)
- Tonnesen, S., & Bryan, G. L. 2009, *ApJ*, 694, 789
- Tonnesen, S., & Bryan, G. L. 2012, *MNRAS*, 422, 1609
- Tonnesen, S., Bryan, G. L., & van Gorkom, J. H. 2007, *ApJ*, 671, 1434
- Tran, K.-V. H., Franx, M., Illingworth, G. D., et al. 2007, *ApJ*, 661, 750
- Tully, R. B., & Shaya, E. J. 1984, *ApJ*, 281, 31
- Urban, O., Werner, N., Simionescu, A., Allen, S. W., Böhringer, H. 2011, *MNRAS*, 414, 2101
- Vollmer, B. 2003, *A&A*, 398, 525
- Vollmer, B., & Huchtmeier, W. 2003, *A&A*, 406, 427
- Vollmer, B., Cayatte, V., Boselli, A., Balkowski, C., & Duschl, W. J. 1999, *A&A*, 349, 411
- Vollmer, B., Marcelin, M., Amram, P., et al. 2000, *A&A*, 364, 532
- Vollmer, B., Cayatte, V., Balkowski, C., & Duschl, W. J. 2001, *ApJ*, 561, 708
- Vollmer, B., Balkowski, C., Cayatte, V., van Driel, W., & Huchtmeier, W. 2004, *A&A*, 419, 35
- Vollmer, B., Huchtmeier, W., & van Driel, W. 2005, *A&A*, 439, 921
- Vollmer, B., Soida, M., Otmianowska-Mazur, K., et al. 2006, *A&A*, 453, 883
- Vollmer, B., Soida, M., Chung, A., et al. 2008a, *A&A*, 483, 89
- Vollmer, B., Braine, J., Pappalardo, C., & Hily-Blant, P. 2008b, *A&A*, 491, 455
- Vollmer, B., Soida, M., Chung, A., et al. 2009, *A&A*, 496, 669
- Vollmer, B., Soida, M., Braine, J., et al. 2012, *A&A*, 537, A143
- von der Linden, A., Wild, V., Kauffmann, G., White, S. D. M., & Weinmann, S. 2010, *MNRAS*, 404, 1231
- Vulcani, B., Poggianti, B. M., Fritz, J., et al. 2015, *ApJ*, 798, 52
- Yagi, M., Yoshida, M., Komiyama, Y., et al. 2010, *AJ*, 140, 1814
- Wang, L., Weinmann, S. M., & Neistein, E. 2012, *MNRAS*, 421, 3450
- Weinmann, S. M., Lisker, T., Guo, Q., Meyer, H. T., & Janz, J. 2011, *MNRAS*, 416, 1197
- Wetzel, A. R., Tinker, J. L., & Conroy, C. 2012, *MNRAS*, 424, 232
- Wetzel, A. R., Tinker, J. L., Conroy, C., & van den Bosch, F. C. 2013, *MNRAS*, 432, 336
- Wheeler, C., Phillips, J. I., Cooper, M. C., Boylan-Kolchin, M., & Bullock, J. S. 2014, *MNRAS*, 442, 1396
- Whitmore, B. C., Gilmore, D. M., & Jones, C. 1993, *ApJ*, 407, 489
- Wijesinghe, D. B., Hopkins, A. M., Brough, S., et al. 2012, *MNRAS*, 423, 3679
- Wolf, C., Aragón-Salamanca, A., Balogh, M., et al. 2009, *MNRAS*, 393, 1302
- Worthey, G. 1994, *ApJS*, 95, 107
- Worthey, G., & Ottaviani, D. L. 1997, *ApJS*, 111, 377
- Wu, P.-F., Gal, R. R., Lemaux, B. C., et al. 2014, *ApJ*, 792, 16

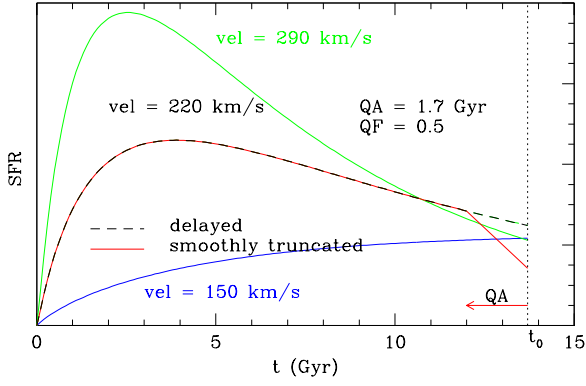


Fig. A.1. The parametric star formation history for a galaxy with a rotational velocity of 220 km s^{-1} (black dashed line), 290 km s^{-1} (green solid line) and 150 km s^{-1} (blue solid line). The black dashed line shows the delayed star formation history given in eq. (1), the red solid line the smoothly declining one (eq. A.1) for a galaxy of rotational velocity 220 km s^{-1} . This figure can be compared to Fig. 2.

Appendix A: Exploring different star formation histories

To test the reliability of the output parameters of the SED fitting code we have also derived the quenching ages and the quenching factors using two other star formation histories. In the first one, we use the same truncated star formation history given in eq. 4 but we leave the rotational velocity of the galaxy as a free parameter and derive $QF(vel)$ and $QA(vel)$. In the second we fix the rotational velocity of the galaxies but we use a smoothly declining star formation history where the decrease of the activity is constant from the beginning of the interaction to the present epoch, as depicted in Fig. A.1 ($QF(SM)$ and $QA(SM)$):

$$SFR(t) = \begin{cases} SFR(t)_{secular} & \text{if } t_0 - t \geq QA \\ SFR(t_0 - QA)_{secular} \\ \times [1 - QF + \frac{QF}{QA} \times (t_0 - t)] & \text{if } t_0 - t < QA \end{cases} \quad (\text{A.1})$$

Figure A.2 shows the relationship between these newly derived parameters and the quenching ages and quenching factors derived in the paper assuming a fixed rotational velocity and the truncated star formation history given in equation 4.

Figure A.2 shows that the quenching factors derived using these three different assumptions on the star formation history and on the rotational velocity of the galaxies are very consistent provided that $QF \gtrsim 0.5$, i.e. in the range of parameters analysed in this work. Figure A.2 also shows that the quenching ages derived using a truncated star formation history (eq. 4) are very consistent regardless the use of a fixed or a variable rotational velocity. This is even clearer whenever the quenching factor is large (the dispersion decreases going from the blue, to the green, the red, and the magenta symbols). On the contrary, there is a systematic shift in the quenching ages when these parameters are derived assuming a truncated or a smoothly declining star formation history, the latter giving systematically larger values (the median values for the $QA(SM)/QA(T)$ are 2.58, 2.80, and 2.98 for the late-type galaxies with $0.5 < QF(T) \leq 0.8$, $QF(T) > 0.8$, and for the early-types, respectively). This is expected since the quenching ages derived using a smoothly declining star forma-

Table A.1. Median quenching ages derived assuming different star formation histories for galaxies with $\chi_r^2 \leq 3$.

Condition	QA(T)	QA(vel)	QA(SM)
	Myr	Myr	Myr
Late-types, $0.5 < QF \leq 0.8$	136	127	302
Late-types, $QF > 0.8$	248	244	423
Early-types ($QF=1$)	1319	614	2997

tion history should be considered as upper limits if the decrease of the activity is more rapid than the one predicted by eq. A.1.

Figure A.3 shows the distribution of the quenching ages derived using a truncated star formation history with the rotational velocity as a free parameter and a smoothly declining star formation history. It can be compared to Fig. 16 derived using a truncated star formation history with fixed rotational velocity. The median values derived for the three different prescriptions are given in Table A.1. The quenching ages derived using a truncated star formation history are very similar regardless the use of a fixed or a variable rotational velocity, with the exception of the early-type sample where the QA is \approx a factor of 2 longer in the former case. The quenching ages derived using a smoothly declining star formation history are, as expected, a factor of ≈ 2 longer than those derived using a truncated star formation activity. The significantly larger number of filled symbols with respect to that of the empty ones in the lower panels of Fig. A.2, indicating those galaxies where the ratio of the reduced χ_r^2 derived from the SED fitting using a truncated to smoothly declining star formation history is smaller than unity ($\chi_r^2(T)/\chi_r^2(SM) < 1$), suggests that the quality of the fit is higher when the truncated approximation is used (the number of free parameters in the two star formation histories are the same). This is also evident in the comparison of Fig. A.3 with Fig. 16 where only galaxies with a reduced $\chi_r^2 \leq 3$ are plotted. The number of galaxies with a good quality fit is larger when a truncated vs. a smoothly declining star formation history is used. A further indication that a truncated star formation history is better suited to trace the evolution of the perturbed Virgo cluster galaxies than the smoothly declining one comes from the comparison of Fig. 12 and Fig. ???. The quenching ages derived using a truncated star formation history with a fixed rotational velocity are those which better reproduce the estimates available in the literature and derived using independent techniques for a dozen of galaxies in common (see sec. 5). Although this small subsample of galaxies is probably biased since composed of systems expressly selected to have some evidence of an undergoing ram pressure stripping event, we decided to adopt a truncated star formation history and a fixed rotational velocity as a reference case for the analysis done in this work. We recall, however, that the quenching ages given by the smoothly declining approximation, which in some cases gives better fits, can be taken as upper limits to the effective time taken by these galaxies to reduce their activity by a factor QF . The timescales to reduce the activity of late-type galaxies by a factor of $QF < 1$ are $\lesssim 500 \text{ Myr}$, and $\lesssim 3 \text{ Gyr}$ (≈ 2 crossing times of the Virgo cluster, Boselli & Gavazzi 2006) to stop the activity and transform late-type galaxies in lenticulars.

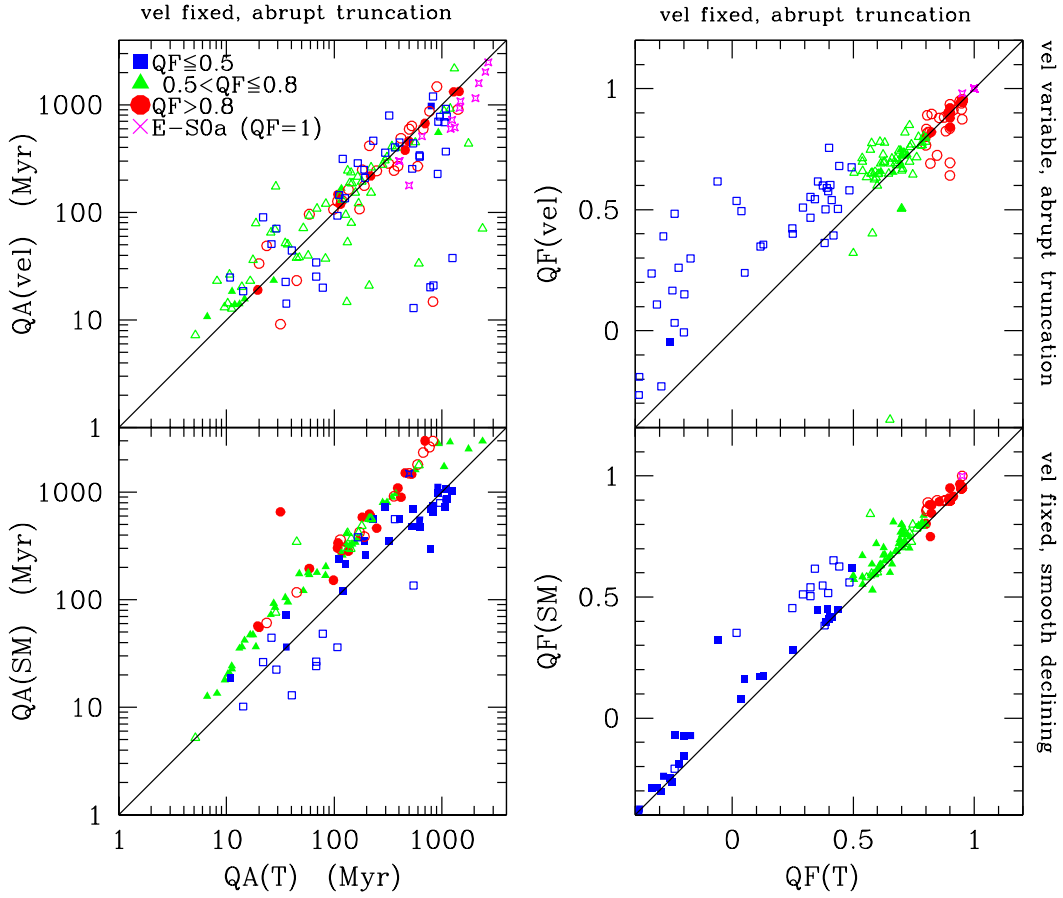


Fig. A.2. Left panel: relationship between the quenching age parameter derived using a truncated star formation history (eq. 4) with the rotational velocity as a free parameter ($QA(vel)$, upper panel) or using a smoothly declining star formation history (eq. A.1) with fixed rotational velocity ($QA(SM)$, lower panel) vs. the one derived using a truncated star formation history (eq. 4) determined using a fixed value for the rotational velocity $QA(T)$. Filled symbols and crosses indicate galaxies where the reduced χ_r^2 in the truncated model with fixed velocity is smaller than the one derived with the smoothly declining star formation history or the truncated one with the rotational velocity as a free parameter, empty symbols for $\chi_r^2(T)/\chi_r^2(SM, vel) > 1$. Blue squares, green triangles, and red circles are for late-type galaxies with a quenching factor $QF \leq 0.5$, $0.5 < QF \leq 0.8$, and $QF > 0.8$, respectively, while the magenta crosses and empty stars for early-type galaxies. The black solid line shows the 1:1 relation. Only galaxies with a $\chi_r^2 \leq 3$ are plotted. Right panel: same relationships for the quenching factor.

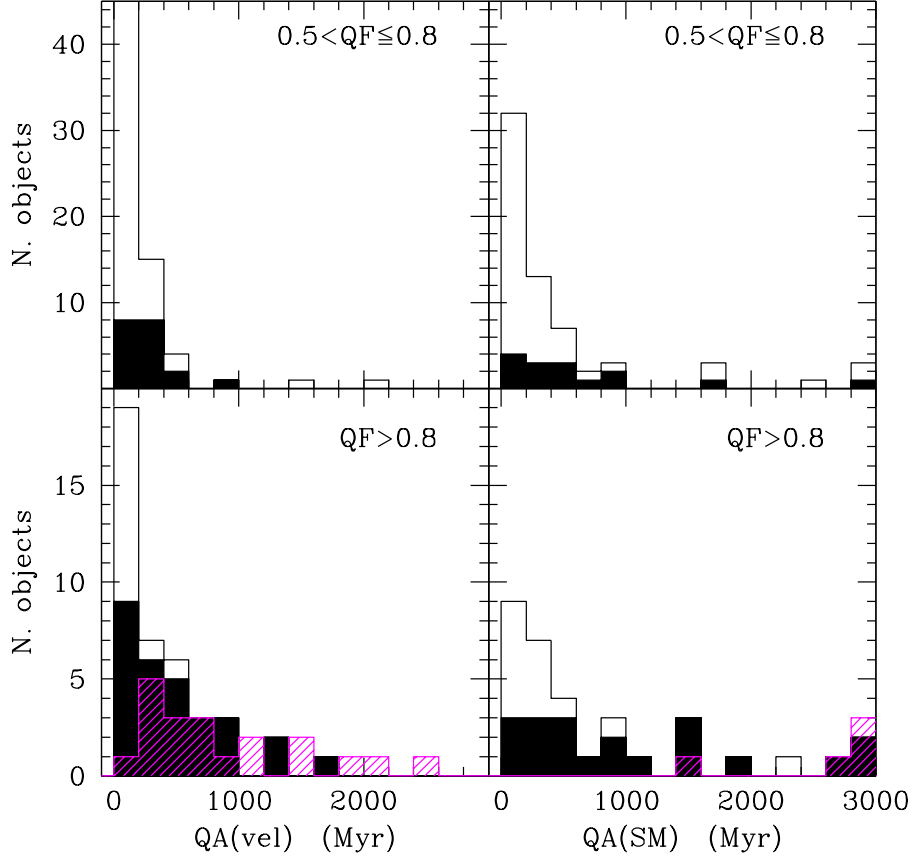


Fig. A.3. Left panels: distribution of the quenching age parameter $QA(vel)$ for galaxies with $\chi_r^2 \leq 3$ and a quenching factor $0.5 < QF(vel) \leq 0.8$ (upper panel) and $QF(vel) > 0.8$ (lower panel) derived using a truncated star formation history (eq. 4) with the rotational velocity as a free parameter. The magenta histogram is for early-type galaxies, the empty histogram for all late-type galaxies, and the black shaded histogram for HI-deficient ($HI - def > 0.4$) late-type systems. Right panels: the same distributions derived using a smoothly declining star formation history (eq. A.1) and a fixed rotational velocity.

